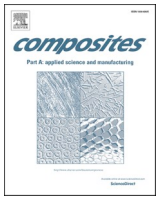
Composites: Part A 203 (2026) 109515



Contents lists available at ScienceDirect

Composites Part A

journal homepage: www.elsevier.com/locate/compositesa



Simulating real FRP microstructures under longitudinal compression: Realistic fibre content, kinking–torsion metrics, and enhanced computational efficiency

D. Bikos [a,c,*], R.S. Trask [b], P. Robinson [c], S. Pimenta [a,*]

[a] Department of Mechanical Engineering, Imperial College London, UK
[b] Bristol Composites Institute, School of Civil, Aerospace and Design Engineering, University of Bristol, Bristol, UK
[c] Department of Aeronautics, Imperial College London, London, UK

ARTICLE INFO

Keywords:
Polymer-matrix composites
Microstructures
Finite element analysis (FEA)
Micromechanics

ABSTRACT

Local imperfections in microstructures are a key factor influencing the compressive performance of fibre-reinforced polymer composites (FRPs); this can be investigated through micromechanical finite element (μFE) simulations of representative volume elements (RVEs) reconstructed from computed tomography of real FRP microstructures. This is the first paper that identifies and addresses three key open challenges in μFE simulations of real FRPs under longitudinal compression: firstly, we introduce a new method for generating continuum μFE models of RVEs with high fibre content (up to 55%) and without unrealistic resin-rich boundaries or fibre interpenetration. Secondly, we propose new microstructural metrics to characterise misalignment and twisting, novel deformation metrics to quantify kinking and torsion during compression, and we analyse their relationships. Thirdly, we validate our recently proposed, computationally efficient, shell-beam (SB) methodology at the microstructural level. The results highlight the importance of simulating FRP microstructures with a realistic fibre content and microstructural twist and demonstrate the very good predictive performance of SB models.

1. Introduction

The longitudinal compressive strength of unidirectional fibre-reinforced polymer composites (FRPs), which is often inferior to tensile strength, is strongly influenced by local microstructural imperfections [1–5]. Understanding the effect of these imperfections, particularly on the sequence of failure events under compression, is essential for improving composite performance and guiding the design of advanced architectures. Realistic micromechanical finite element models (μFEM), using fibre paths reconstructed from micro-computed tomography of FRP samples (μCT-RVEs), are often proposed to investigate the effect of real composite imperfections on FRP's compressive strength [6–8]. In principle, μCT-RVEs provide an accurate representation of the fibre and matrix architecture at a sufficiently fine scale to enable the simulation of the complete sequence of failure events under compression while resolving detailed local stress and strain fields within the constituents and their interactions. However, three key challenges have so far limited the success of this approach, as outlined next.

Firstly, all simulated μCT-RVEs so far [6–9] have fibre volume fractions (between V^f = 9.1–51.1 %) significantly lower than those of the experimental samples. This reduction arises partially from idealising RVEs as perfectly prismatic volumes (with circular or square cross-sections) and deleting all fibres intersecting the RVE's lateral boundaries; this creates unrealistic resin-rich zones [6–9]. In addition, the fibre diameter is usually reduced [6,7,9] to avoid spurious interpenetration of neighbouring fibres. Fibre interpenetrations are likely caused by limitations in μCT image resolution (typically 0.48–0.78 μm for carbon FRPs [10,11]), uncertainties in the fibre-tracking algorithms (e.g., centre detection accuracy), and variability in fibre diameter (typical coefficient of variation for carbon fibres of 4.6–6.7 % [12]). These effects, combined with the fact that real fibres are often non-circular [8,10] (a feature largely overlooked in the literature), contribute to the fibre content inconsistencies observed in μCT-RVEs. To date, only one study [8] has considered variability of fibre diameters in μCT-RVEs, by imposing an artificial distribution of fibre diameters with a controlled mean and standard deviation; but unfortunately, the RVE still had spurious resin

* Corresponding authors.
E-mail addresses: d.bikos17@imperial.ac.uk (D. Bikos), soraia.pimenta@imperial.ac.uk (S. Pimenta).

https://doi.org/10.1016/j.compositesa.2025.109515
Received 29 August 2025; Received in revised form 11 December 2025; Accepted 13 December 2025
Available online 17 December 2025
1359-835X/© 2025 The Authors. Published by Elsevier Ltd. This is an open access article under the CC BY license (http://creativecommons.org/licenses/by/4.0/).

rich zones at the lateral boundaries.

Secondly, there is a need to better relate the effect of different microstructural imperfections and their length-scales on the compressive response of FRPs. Fibre misalignment is known to be critical, as it couples longitudinal compression with longitudinal–transverse shear. This triggers shear instability of the matrix in the inter-fibre space, allowing fibres to bend locally and leading to kink-band formation [3,13–16]. In contrast, the effect of microstructural twisting, i.e. a coordinated helical motion of groups of fibres [17], has been severely overlooked. A torsional deformation of specimens during longitudinal compression has been recently observed experimentally [1,8] and numerically [8,9] in μCT-RVEs; however, its connection to an initial microstructural twist in the fibre architecture has not been investigated. Only one study [1] has highlighted the critical role of torsional deformations (~2.2° over ~ 1400 μm, and for a volume containing 5229 fibres) in kink-band formation and its potential link to manufacturing-induced microstructural twist, although this twist was not directly quantified. Hence, the relationships between microstructural twist, torsional motion under compression, and their interaction with kinking remain unquantified and unexplored.

Thirdly, μCT-RVE FE simulations are limited by extremely high computational cost. Typical analyses can require several weeks and yet are often restricted to small, simulated domains containing only a few dozen fibres, up to 400 μm long. These small-scale models are prone to global buckling effects [6–9], and lack the microstructural variability needed to be statistically representative [4].

In our previous work [9], we introduced a new computationally-efficient micromechanical finite element (μFE) methodology that simulates matrix and fibres using shell and beam (SB) elements respectively. When compared to the conventional continuum-element based (CC) approach, the SB methodology reduced the simulation time by over 99.9 % and predicted the compressive strength with at least 94 % accuracy. In addition to improvement in computational cost, the SB methodology inherently avoids the spurious creation of resin-rich zones at the lateral boundary of μCT-RVEs, since it does not require a cylindrical or prismatic cross-section; however, in our previous work [9], this created a discrepancy between the SB and the CC simulations, which did not allow for a full validation of the former, especially at the microscale.

In this paper, we address these three challenges in μCT-RVE FE simulations. We first present the μCT-RVE selected from a literature dataset (Section 2) and outline the key FE simulation parameters, including the constitutive laws and boundary conditions (Section 3). Then, in Section 4, we introduce new metrics to decouple the effects of fibre misalignment, twist, and local variability, examine their role in kinking and torsional motions, and relate them to the compressive response. In Section 5, we propose a μCT-RVE methodology with continuum finite-elements capable of achieving realistic fibre volume fractions without resin-rich boundaries or fibre interpenetrations. In Section 6, we validate the computationally efficient shell–beam (SB) approach against these continuum μFEM, both at macro- and micro-scales. We then discuss the key mechanisms and the sequence of failure events under longitudinal compression, and analyse the current limitations and opportunities in μCT-RVE FE simulations (Section 7), before summarising the main conclusions (Section 8).

2. Microstructure

2.1. Original μCT dataset

This paper uses a carbon/epoxy μCT-RVE generated from an available fibre-path dataset tracked experimentally by Emerson *et al.* [10]. The composite was manufactured through filament winding and vacuum infusion; overall properties are shown in Table 1.

Table 1
Properties of the original carbon/epoxy composite as obtained experimentally [10]. Further details about the experimental distribution of fibre misalignments are provided in Emerson et al. [10], whilst our definition and computation of fibre misalignment angles are described in Section 4.1.

Property	Variable & Value
Average fibre diameter	$\overline{\phi}^{\mathrm{f}}_{\mathrm{exp}} = 7\mu\mathrm{m}$
Average fibre volume fraction	$\overline{V}^{\mathrm{f}}_{\mathrm{exp}} = 53.0 \pm 0.3\%$
Average fibre misalignment angle	$\overline{\theta}_{\mathrm{exp}} = 1.61^{\circ}$
Experimentally measured compressive strength	$X^{\mathrm{RVE}}_{\mathrm{c,exp}} = 900 \pm 60$ MPa
Voxel size of original CT scan dataset	0.482 μm

2.2. Selection of fibre paths for μCT-FEM

A μCT-RVE with a total of $N_{\mathrm{f}} = 98$ fibres and a length $L = 350$ μm was isolated from the original dataset of fibre paths [10], as shown in Fig. 1, where the overall longitudinal direction of the original dataset is aligned with the z-axis. The fibre-path data in the selected μCT-RVE consist of $x_{i,j}$ and $y_{i,j}$ fibre centres coordinates, where:

- Variable $i = \{1, \cdots, N_{\mathrm{f}} = 98\}$ identifies each fibre's ID;
- Variable $j = \{1, \cdots, N_z\}$ identifies each transverse cross-section (at a longitudinal position $z = z_j$), sampled with a uniform spacing $\Delta z = 1\mu$m (z-intervals of the original dataset).

The μCT-RVE fibre paths were smoothed and down-sampled from the original dataset to $\Delta z = \overline{\phi}^{\mathrm{f}} = 7\mu$m(using MATLAB's "*smoothdata*" function with a "*lowess*" filter and a window size $\overline{\phi}^{\mathrm{f}}$), resulting in $N_z = 51$ transverse sections. This window size was chosen because it successfully removed the high-frequency oscillations in the μCT data, is consistent with the element size (along the fibre length direction) that will be used in the SB FE simulations (in Section 6), and is linked to a physical dimension that should act as a lower bound for the wavelength of fibre waviness ($\overline{\phi}^{\mathrm{f}}$). This choice will be further corroborated by the statistical analysis of fibre misalignments (in Section 4.1.1. Fig. 4), where the statistical distributions of misalignments sampled globally (over the full length L) and locally (along the spacing Δz) are relatively similar (meaning that further increasing Δz, as done in the literature [10,11], would have a very small effect on the local distribution only).

The location and size of the μCT-RVE were selected based on the following criteria:

a. A volume small enough to be simulated in a reasonable simulation time (e.g., maximum 6 days using the computer specifications in Section 5.3), through conventional μFE modelling with continuum elements;
b. A length sufficiently short to avoid global buckling, based on estimates from the Euler buckling load and from the linear-elastic simulations presented in Supplementary Material (Section 1.4).
c. A region with frequent changes in fibre neighbourhood (as depicted in Fig. 2);
d. A region with an average fibre misalignment similar to the global value reported for the original dataset (i.e., 1.61° in Table 1)[10], along with a sufficiently broad distribution of misalignment angles (as characterised in Section 2.2) and noticeable local variations in fibre content;
e. A region with a mostly circular cross-section to facilitate the generation of μFEM with continuum elements (see Section 5).

The selection of the μCT-RVE was based on these criteria was achieved through manual inspection of the reconstructed microstructure. Criteria (c)–(d) were imposed to demonstrate the effectiveness of the FE modelling approaches to deal with the complexity of realistic fibre paths with typical microstructural features observed in larger volumes. In any

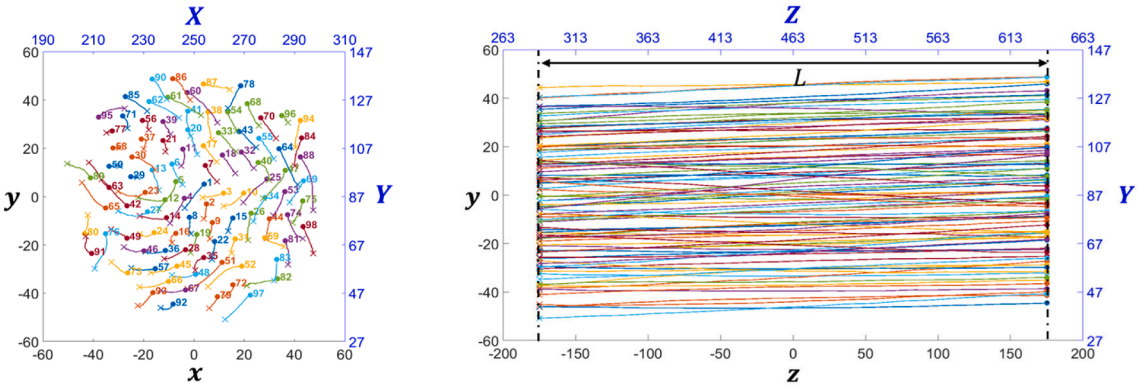


Fig. 1. Fibre paths in the selected μCT-RVE. The numbers next to the fibre paths in Subfigure b represent the variable i that identifies each fibre. The global coordinates in the original μCT dataset are X, Y, Z, while the local coordinates of the selected μCT-RVE are shifted to x, y, z (all in μm).



Fig. 2. Position of fibre centres (with fibre ID (i) shown) and corresponding alpha triangulation (with $a = 10.69$μm) for three z−sections. Changes in fibre neighbourhood between these three adjacent sections, i.e. connectivities present in one section but absent in the previous or next section, are shown in red.

case, comparisons between predicted mechanical properties and experimental data should be interpreted with caution since (i) the selected μCT-RVE may not be statistically representative of the entire material and (ii) the full dataset (in Fig. 1a) itself corresponds to only 0.08 % of the tested gauge volume of the specimens from which the experimental properties were determined [10].

Fig. 2 illustrates the centre positions of the 98 fibres at three distinct z-sections, along with the alpha triangulation connecting neighbouring fibre centres (generated using the MATLAB function "*alphaShape*" [18]). The alpha triangulation is a non-convex generalisation of the Delaunay triangulation, thus allowing for re-entrant features at the boundary, whose extent is controlled by a user-specified alpha radius, $0 < a < \infty$, as further discussed in Section 5.

3. Numerical modelling

3.1. Constitutive laws

The fibre are assumed axisymmetric around the local fibre direction (1), with an isotropic Poisson's ratio ($\nu^{\mathrm{f}}_{12}=\nu^{\mathrm{f}}_{13}=\nu^{\mathrm{f}}_{23}=\nu^{\mathrm{f}}$) independent of the applied strain, as defined in Table 2. Their longitudinal response was assumed as non-linear elastic up to failure, with a quadratic stress–strain (σ^{f}_{11} vs. $\varepsilon^{\mathrm{f}}_{11}$) relationship:

$$\sigma^{\mathrm{f}}_{11}\left(\varepsilon^{\mathrm{f}}_{11}\right) = E^{\mathrm{f}}_{11,0}\varepsilon^{\mathrm{f}}_{11} + \frac{\Delta E^{\mathrm{f}}_{11}}{2}{\varepsilon^{\mathrm{f}}_{11}}^{2}, \; -X^{\mathrm{f}}_{\mathrm{c}} \le \sigma^{\mathrm{f}}_{11} \le X^{\mathrm{f}}_{\mathrm{t}}, \tag{1}$$

where the initial modulus ($E^{\mathrm{f}}_{11,0}$), the quadratic coefficient ($\Delta E^{\mathrm{f}}_{11}$), and the tensile strength ($X^{\mathrm{f}}_{\mathrm{t}}$) were obtained from single-fibre tensile tests on T300 fibres [12], while the compressive strength ($X^{\mathrm{f}}_{\mathrm{c}}$) was assumed as a commonly reported value in the literature for T300 fibres [6,19].

The quadratic expression of Eq. (1) was fitted to the experimentally measured tensile behaviour for T300 fibres, which exhibit an approximately linear increase in elastic modulus with strain [12]; the expression was then extrapolated to the compression regime to ensure continuity at zero strain. Beyond the corresponding longitudinal strains at peak ($\varepsilon^{\mathrm{f}}_{11,X_{\mathrm{t}}}$ under tension and $\varepsilon^{\mathrm{f}}_{11,X_{\mathrm{c}}}$ under compression shown in Table 2), the longitudinal modulus at peak was linearly degraded by a factor of 10^3 over a 1 % relative increase in strain (i.e. between the strain at peak and $\varepsilon^{\mathrm{f}}_{11,\mathrm{ft}} = 1.01\varepsilon^{\mathrm{f}}_{11,X_{\mathrm{t}}}$ or $\varepsilon^{\mathrm{f}}_{11,\mathrm{fc}} = 1.01\varepsilon^{\mathrm{f}}_{11,X_{\mathrm{c}}}$), thus simulating fibre failure. The full nonlinear σ^{f}_{11} vs. $\varepsilon^{\mathrm{f}}_{11}$ curve is shown in Fig. 3a, with parameters defined in Table 2.

A proportionally similar strain-dependent relationship was applied to the remaining fibre moduli, E^{f}_{22}, G^{f}_{12}, and G^{f}_{23}, by using the same longitudinal strain-based scaling factor as for E^{f}_{11}. In the μFEM, this nonlinearity was implemented by assigning all local moduli as dependent on the local longitudinal strain, using Abaqus' keyword **User defined field, type = specified* [21].

The epoxy matrix was modelled with a linear-elastic-nonlinear-plastic response (Fig. 3b), based on experimental shear data for EPON 682 [16]. The initial linear elastic response was defined by the Young's modulus (E^{m}) and Poisson's ratio (ν^{m}) shown in Table 2, with a shear

Table 2
Constituent properties for the μFEM with continuum elements (uncalibrated properties) [12,19,20]. The full matrix plasticity hardening data are summarised in Supplementary Material (Section 1.3).

	Material Property	Variable & value
Fibre (T300)	Longitudinal Young's modulus at $\varepsilon^{f}_{11} = 0$	$E^{f}_{11,0} = 226.5$GPa
	Rate of longitudinal stiffness	$\Delta E^{f}_{11,0} = 4240$GPa
	Longitudinal tensile strength ($L = 0.35$ mm)	$X^{f}_{t} = 7353$GPa
	Longitudinal tensile strain at peak	$\varepsilon^{f}_{11,X_t} = 2.61\%$
	Longitudinal compressive strength	$X^{f}_{c} = 3700$GPa
	Longitudinal compressive strain at peak	$\varepsilon^{f}_{11,X_c} = 2.01\%$
	Transverse Young's moduli at $\varepsilon^{f}_{11} = 0$	$E^{f}_{22,0} = E^{f}_{33,0} = 27.6$GPa
	Longitudinal Shear moduli at $\varepsilon^{f}_{11} = 0$	$G^{f}_{12,0} = G^{f}_{13,0} = 10.9$GPa
	Poisson's ratio (independent of strain)	$\nu^{f} = 0.3$
Matrix (EPON 682)	Young's modulus	$E^{m} = 2900$MPa
	Poisson's ratio	$\nu^{m} = 0.4$
	Initial yield stress ("o" in Fig. 3b)	$\sigma^{m}_{p,o} = 47.6$MPa
	Yield stress at first local peak ("peak" in Fig. 3b)	$\sigma^{m}_{p,peak} = 95.3$MPa
	Yield strain at first local peak ("peak" in Fig. 3b)	$\varepsilon^{m}_{p,peak} = 0.110$
	End yield stress point ("end" in Fig. 3b)	$\sigma^{m}_{p,end} = 100.5$MPa
	End yield strain point ("end" in Fig. 3b)	$\varepsilon^{m}_{p,end} = 0.375$

modulus G^{m} calculated using Eq. (2).

The nonlinear plastic response was modelled through J2 (von Mises) plasticity with isotropic hardening. The hardening curve was implemented in Abaqus in tabular form (Supplementary Material, Section 1.3); the yield stress (σ^{m}_{p}) vs plastic strain (ε^{m}_{p}) values were converted from the shear data (shown in Fig. 3b), using Eq. (2). The initial yield point ($\sigma^{m}_{p,o}$), first local peak values ($\sigma^{m}_{p,peak}$ and $\varepsilon^{m}_{p,peak}$), and yield point at the end of the measured constitutive law ($\sigma^{m}_{p,end}$ and $\varepsilon^{m}_{p,end}$) are summarised in Table 2.

$$G^{m} = \frac{E^{m}}{2(1+\nu^{m})}, \sigma^{m}_{p} = \sqrt{3}\tau^{m}_{p}, \varepsilon^{m}_{p} = \frac{\gamma^{m}_{p} - \frac{\tau^{m}_{p}}{G^{m}}}{\sqrt{3}}. \quad (2)$$

This von Mises plasticity model, based on bulk-epoxy data, ignores pressure-dependency and dilatancy of the matrix, as well as *in-situ* curing effects; these simplifications are common in the literature [6,9,22], and further discussed in Section 7.2.

An additional μCT-RVE simulation (Supplementary Material, Section 1.4) using a purely linear elastic matrix confirmed that the μCT-RVE response was governed primarily by matrix plasticity rather than global elastic buckling.

3.2. Boundary conditions

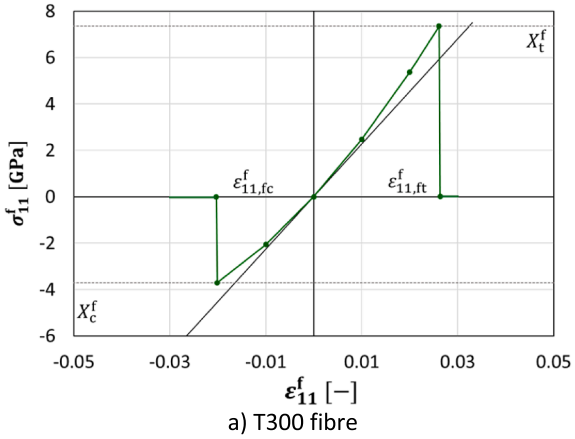
Longitudinal compression was applied to the μCT-RVE through a velocity-controlled boundary condition at the front end ($z = L/2$), while the back end ($z = -L/2$) was constrained in the z-direction. To prevent rigid body translation and rotation, two additional nodes on $z = -L/2$ (Q_1 at the centre, and Q_2 with the same y-coordinate), were also constrained. These boundary conditions (BCs) are commonly used in the literature [6,8,9] and are defined as follows:

$$\text{Front end}: \quad z = +\frac{L}{2} : \dot{w} = 1, \quad (3)$$

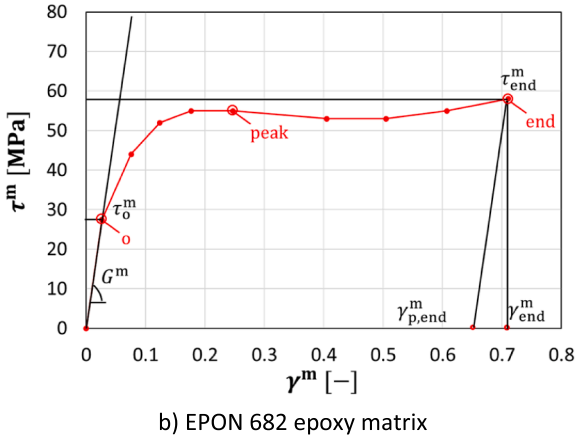
$$\text{Back end}: \quad z = -L/2 : w(x, y, z = 0) = 0, \{u, v\}(Q_1) = 0, v(Q_2) = 0 \quad (4)$$

where u, v, w represent displacements in the $x-, y-,$ and $z-$ directions, respectively.

No constraints were imposed on the lateral faces of the μCT-RVE, which remained free to move. While such BCs neglect the influence of the surrounding material (i.e., neighbouring regions of the UD specimen or adjacent plies), implementing an appropriate strategy to account for this influence is not trivial: for instance, introducing a homogenised surrounding material would require arguably arbitrary decisions about



a) T300 fibre



b) EPON 682 epoxy matrix

Fig. 3. Nonlinear stress–strain constitutive response of composite constituents [12,20]. The scatter on the curves represents the data points used as inputs in Abaqus (for the matrix, this required converting to yield stresses and plastic strains using Eq. (2), and the labelled points are referred throughout the text).

the ideal size, misalignment field, and homogenised properties for that region (this is further discussed in Section 7.2.i and 7.2.iii); alternatively, applying periodic boundary conditions (PBCs) would impose an artificial, infinite repetition of fibre paths, inconsistent with the inherent variability observed experimentally in μCT datasets.

3.3. Simulation outputs

The results from μFE simulations are presented as defined below (subscript "t" identifies the simulation increment, and superscript "RVE" indicates an overall μCT-RVE quantity).

3.3.1. Global stress–strain response

The remote longitudinal stress–strain response ($\sigma_{zz}^{\mathrm{RVE}} - \varepsilon_{zz}^{\mathrm{RVE}}$) of the μCT-RVE is computed as:

$$\sigma_{zz}^{\mathrm{RVE}} = \frac{\mathrm{F}_{\mathrm{zz,t}}^{\mathrm{RVE}}}{(\sum_{\mathrm{i}=1}^{\mathrm{N^f}} \pi \phi_{\mathrm{i}}^{\mathrm{f}^2}/4)/\mathrm{V}_{\mathrm{CAE}}^{\mathrm{f}}}, \tag{5}$$

$$\varepsilon_{zz}^{\mathrm{RVE}} = \frac{w_t^{\mathrm{RVE}}}{L}, \tag{6}$$

where $F_{zz,t}^{\mathrm{RVE}}$ is the total reaction force at front end ($z = L/2$), w_t^{RVE} is the displacement in the longitudinal direction at $z = L/2$, and $V_{\mathrm{CAE}}^{\mathrm{f}}$ is the fibre volume fraction obtained using Abaqus CAE "*mass-properties*" tool (shown in Table 3, Section 5.3).

3.3.2. Local strain fields

Results concerning matrix yielding are expressed as equivalent plastic strain, $\varepsilon_{\mathrm{eq,p}}^{\mathrm{m}}$, extracted from matrix locations corresponding to the integration points of the shell elements in the SB-RVEs (details of the SB meshing are given in Fig. 14). This allows direct comparison between CC-RVEs and SB-RVEs, discussed in Section 6. Fibre response is represented by the longitudinal strain, $\varepsilon_{11}^{\mathrm{f,env}}$, corresponding to the maximum absolute value across the beam's section points (envelope).

4. Metrics for combined analysis of microstructures and micromechanical deformation modes

4.1. Microstructural metrics

In this section, microstructural and micromechanical metrics are defined at three levels:

- Local metrics (superscript "f", subscripts "i,j"), for individual sections (of length Δz) of individual fibres;
- Fibre metrics (superscript "f", subscript "i"), along the full length (L) of individual fibres;
- RVE metrics (superscript "RVE"), for the overall deformation of the RVE.

4.1.1. Fibre-based misalignment metrics

The misalignments of the fibres in the μCT-RVE are characterised through two angles, the misalignment magnitude:

$$\theta_{0,i}^{\mathrm{f}} = \mathrm{atan}\left(\frac{\sqrt{\Delta x_{0,i}{}^2 + \Delta y_{0,i}{}^2}}{L}\right), \quad \theta_{0,ij}^{\mathrm{f}} = \mathrm{atan}\left(\frac{\sqrt{\Delta x_{0,ij}{}^2 + \Delta y_{0,i}{}^2}}{\Delta z}\right), \tag{7}$$

and the misalignment phase (relatively to the y-direction, equivalent to the azimuth angle):

$$\varphi_{0,i}^{\mathrm{f}} = \mathrm{atan}\left(\frac{\Delta x_{0,i}}{\Delta y_{0,i}}\right), \quad \varphi_{0,ij}^{\mathrm{f}} = \mathrm{atan}\left(\frac{\Delta x_{0,ij}}{\Delta y_{0,ij}}\right). \tag{8}$$

These definitions distinguish between full-fibre and local misalignments of each fibre i:

- Full-fibre misalignments are calculated between the back ($j = 1$) and front ($j = N_z$) sections (so along a z-distance L), with $\Delta x_{0,i} = x_{0,ij=N_z} - x_{0,ij=1}$ (and similarly defined $\Delta y_{0,i}$);
- Local misalignments are calculated between consecutive sections j and $j+1$ (so along a z-distance $\Delta z = \overline{\phi}^{\mathrm{f}}$), with $\Delta x_{0,ij} = x_{0,ij+1} - x_{0,ij}$ (and similarly defined $\Delta y_{0,ij}$).

Since the subscript "0" indicates the undeformed state of the μCT-RVE, each vector $\Delta_{0,i,(j)}^{\mathrm{f}} = \left(\Delta x_{0,i,(j)}, \Delta y_{0,i,(j)}\right)$ represents the microstructural imperfection of fibre i.

The distributions of full-fibre and local misalignments for the 98-fibres μCT-RVE are presented in Fig. 4a-d, including key statistical metrics. For the misalignment magnitudes, which are directionless and small ($\theta_{0,i,(j)}^{\mathrm{f}} \leq 10^{\circ}$), the arithmetic mean and standard deviation are shown. For the misalignment phase, which can take values in the entire range $0^{\circ} \leq \varphi_{0,i,(j)}^{\mathrm{f}} \leq 360^{\circ}$, the circular mean:

$$\overline{\varphi_{0,i,(j)}^{\mathrm{f}}} = \mathrm{atan}\left(\frac{\sum \sin(\varphi_{0,i,(j)}^{\mathrm{f}})}{\sum \cos(\varphi_{0,i,(j)}^{\mathrm{f}})}\right), \tag{9}$$

best represent the central tendency, while the circular interquartile distance (IQD [23], computed as the minimum arc length that contains 50 % $\varphi_{0,i,(j)}^{\mathrm{f}}$ data about the circular mean) best represents dispersion.

4.1.2. RVE-based misalignment metrics

Like the metrics defined in Section 4.1.1. for individual fibres, the overall misalignment magnitude and phase of the μCT-RVE can be characterised by the following equivalent metrics:

$$\theta_0^{\mathrm{RVE}} = \mathrm{atan}\left(\frac{\sqrt{\Delta x_0^{\mathrm{RVE}2} + \Delta y_0^{\mathrm{RVE}2}}}{L}\right), \quad \varphi_0^{\mathrm{RVE}} = \mathrm{atan}\left(\frac{\Delta x_0^{\mathrm{RVE}}}{\Delta y_0^{\mathrm{RVE}}}\right), \tag{10}$$

where $\Delta x_0^{\mathrm{RVE}} = \overline{\Delta x_{0,i}}$ and $\Delta y_0^{\mathrm{RVE}} = \overline{\Delta y_{0,i}}$. The values of θ_0^{RVE} and φ_0^{RVE} are shown in Fig. 4e-f; note that these misalignment metrics quantify the *coordinated* misalignment of the overall RVE, and are therefore naturally different from the fibre-/local-based means ($\overline{\theta_{0,i,(j)}^{\mathrm{f}}}$ and $\overline{\varphi_{0,i,(j)}^{\mathrm{f}}}$).

4.1.3. New metric to characterise RVE twisting

To quantify the overall level of twisting imperfections of the μCT-RVE, we propose a new metric: the RVE twisting angle, denoted as ψ_0^{RVE}. The RVE twisting angle is calculated using MATLAB's "*Procrustes*" function [18]; this is based on the orthogonal Procrustes analysis [24], which identifies the rigid-body transformation (with rotation and translation components, but no scaling nor reflections) that best aligns two corresponding sets of points (by minimising the sum of squared errors). Here, the input sets of points are the fibre centres at the back ($x_{0,ij=1}, y_{0,ij=1}$) and front ($x_{0,ij=N_z}, y_{0,ij=N_z}$) sections, as shown in Fig. 5.

The Procrustes analysis returns a rotation matrix $\left[\Psi_0^{\mathrm{RVE}}\right]$ (corresponding to a rotation or twisting angle ψ_0^{RVE}) and a translation vector $\Delta_0^{\mathrm{RVE}} = (\Delta x_0^{\mathrm{RVE}}, \Delta y_0^{\mathrm{RVE}})$(coincident with the components used in Eq. (10)), from which the total imperfection of each individual fibre (i.e. each vector $\Delta_{0,i}^{\mathrm{f}} = (\Delta x_{0,i}, \Delta y_{0,i})$) is decomposed into three distinct components:

- A translational component $\Delta_{0,i}^{\mathrm{f,tra}} = \Delta_0^{\mathrm{RVE}}$ (uniform for all fibres), which characterises the overall misalignment of the μCT-RVE;
- A rotational component $\Delta_{0,i}^{\mathrm{f,rot}} = \left[\Psi_0^{\mathrm{RVE}}\right] \cdot (x_{0,ij=1} - \overline{x_{0,ij=1}}; y_{0,ij=1} - \overline{y_{0,ij=1}})$, which characterises the twisting of the μCT-RVE;

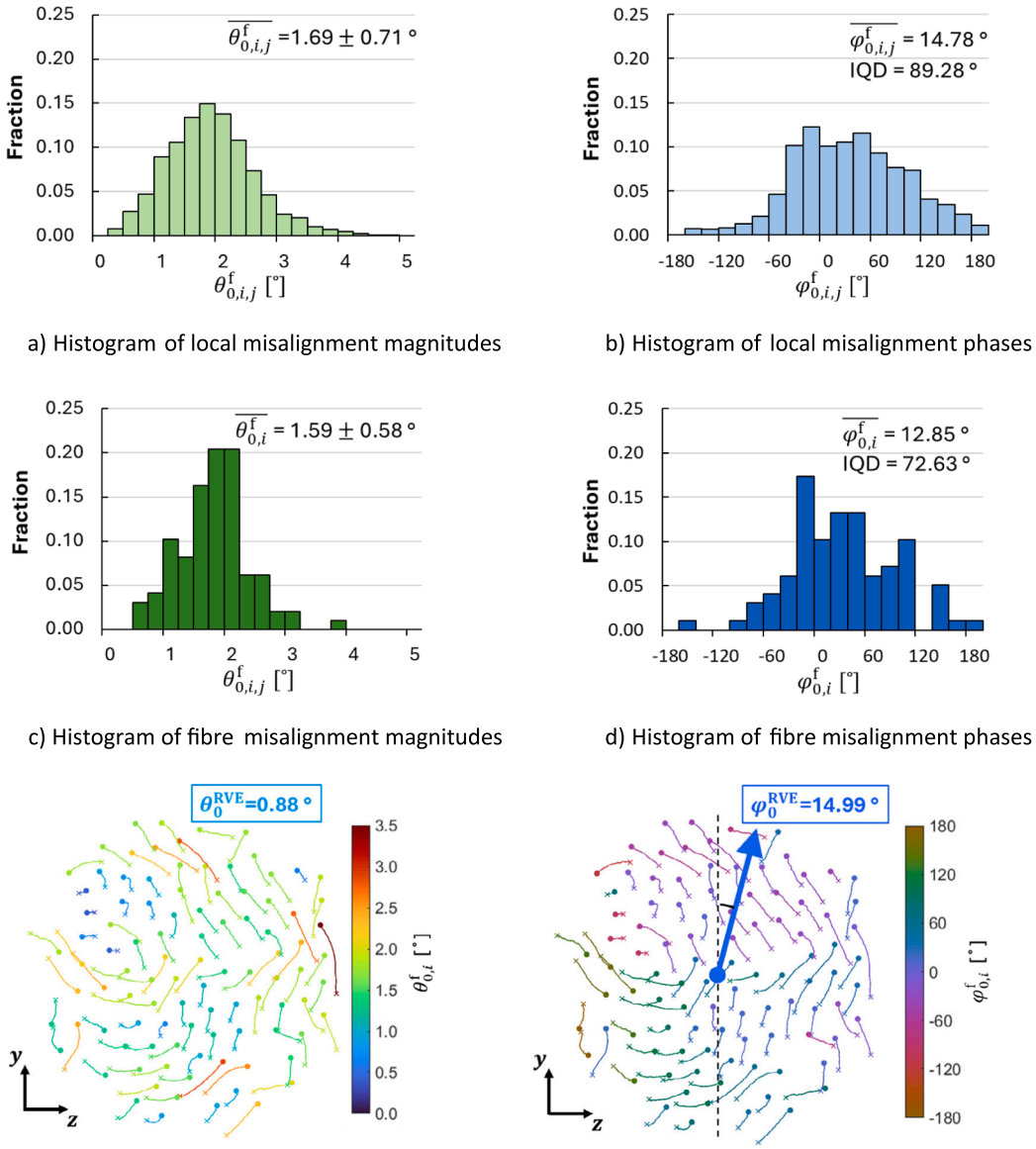


Fig. 4. Characterisation of misalignments of the μCT-RVE with 98 fibres. Key statistics of the distributions are shown at the top of each histogram (a-d): the arithmetic mean and standard deviation for $\theta^{f}_{o,i}$, $\theta^{f}_{o,i,j}$, and circular mean (Eq. (9)) and interquartile distance (IQD) [23] for $\varphi^{f}_{o,i}$, $\varphi^{f}_{o,i,j}$. In Subfigures e and f, the start and the end of the fibre are denoted with "x" and "●" respectively, and θ_0^{RVE} and φ_0^{RVE} refer to the RVE misalignment and phase (as described in Section 4.1.2).

- A residual component $\Delta^{f,res}_{0,i} = \Delta^{f}_{0,i} - \left(\Delta^{f,tra}_{0,i} + \Delta^{f,rot}_{0,i}\right)$, which characterises the individual fibre imperfection (decoupled from the overall coordinated RVE misalignment and twisting).

This decomposition of fibre imperfection components is illustrated in Fig. 5 for the μCT-RVE analysed. The RVE twisting angle is $\psi_0^{RVE} = 9.8^{\circ}$; the relevance of this large value will be discussed in Section 5.5. The mean magnitudes of the rotational, translational, and residual components of fibre imperfections are very similar, indicating that none can be considered negligible.

4.2. Micromechanical deformation metrics

Building on the metrics defined in Section 4.1 to characterise the microstructure, in this section we propose analogous metrics to characterise the micromechanical deformation. These metrics are based on the transverse displacements $u^{f}_{t,i,(j)}$ and $v^{f}_{t,i,(j)}$ of fibre nodes at a given loading increment t, and decouple translational (labelled as *kinking*) and rotational (labelled as *torsion*) motions.

4.2.1. Fibre-based metrics

We define the kinking magnitude ($\theta^{f}_{t,i,(j)}$) and kinking phase ($\varphi^{f}_{t,i,(j)}$) of individual fibre i at a given increment t in an analogous way to the fibre misalignments in Eqs. (7)-(8):

$$\theta^{f}_{t,i,(j)} = \operatorname{atan}\left(\frac{\sqrt{\Delta u^{f}_{t,i,(j)}{}^{2} + \Delta v^{f}_{t,i,(j)}{}^{2}}}{L}\right) \tag{11}$$

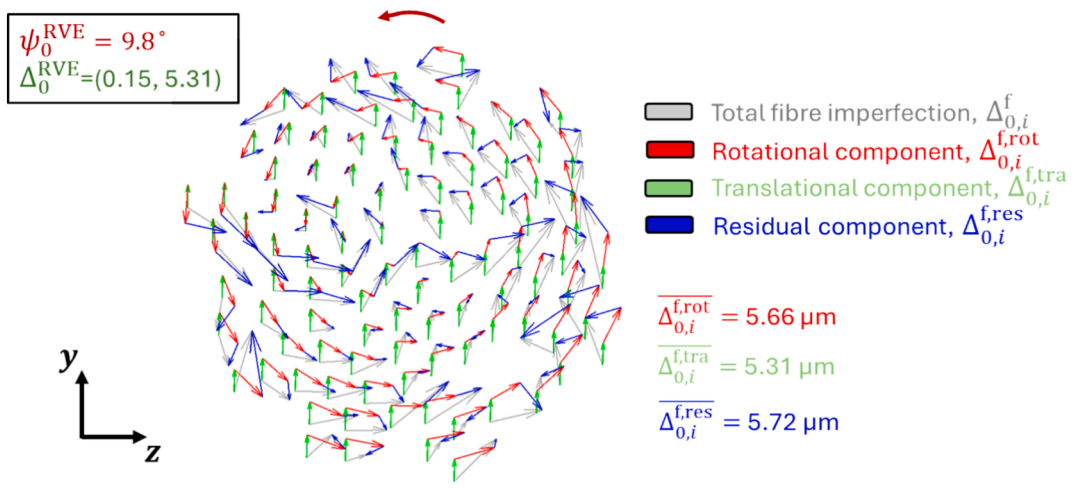


Fig. 5. Decomposition of the fibre imperfection vectors $\Delta_{0,i}^{f} = (\Delta x_{0,i}, \Delta y_{0,i})$ between back ($j = 1$) and front ($j = N_z$) sections using the Procrustes analysis.

$$\varphi_{t,i,(j)}^{f} = \text{atan}\left(\frac{\Delta u_{t,i,(j)}^{f}}{\Delta v_{t,i,(j)}^{f}}\right) \tag{12}$$

These can be computed either at the full-fibre scale (subscript j omitted, with $\Delta u_{t,i}^{f} = u_{t,i,j=N_z}^{f} - u_{t,i,j=1}^{f}$ and similarly defined $\Delta v_{t,i}^{f}$) or at the local scale (with $\Delta u_{t,i,j}^{f} = u_{t,i,j+1}^{f} - u_{t,i,j}^{f}$ and similarly defined $\Delta v_{t,i,j}^{f}$).

4.2.2. New metrics to characterise RVE kinking

We characterise the μCT-RVE kinking deformation by the magnitude (θ_t^{RVE}) and the phase (φ_t^{RVE}) angles, defined in an analogous way to the RVE misalignment in Eq. (10):

$$\theta_t^{RVE} = \text{atan}\left(\frac{\sqrt{u_t^{RVE\,2} + v_t^{RVE\,2}}}{L}\right) \tag{13}$$

$$\varphi_t^{RVE} = \text{atan}\left(\frac{u_t^{RVE}}{v_t^{RVE}}\right), \tag{14}$$

where $u_t^{RVE} = \overline{u_{t,i,j=N_z}^{f}}$ and $v_t^{RVE} = \overline{v_{t,i,j=N_z}^{f}}$ (computed at the RVE's front end ($z = L/2$) due to the BCs that constrain the rigid body motion at the back end of the RVE). Instantaneous values of the phase angle ($\varphi_{inst,t}^{RVE}$) can be obtained by replacing the total displacements u_t^{RVE} and v_t^{RVE} with their change during the FE increment: $\delta u_t^{RVE} = u_t^{RVE} - u_{t-1}^{RVE}$ and $\delta v_t^{RVE} = v_t^{RVE} - v_{t-\delta t}^{RVE}$.

The shear strain equivalent associated with the kinking motion, $\gamma_t^{RVE,kink}$, is defined as follows:

$$\gamma_t^{RVE,kink} = \tan(\theta_t^{RVE}) = \frac{\sqrt{u_t^{RVE\,2} + v_t^{RVE\,2}}}{L}. \tag{15}$$

4.2.3. New metrics to characterise RVE torsion

We propose two new metrics to quantify the global torsional deformation of the RVE. The overall torsion angle of the RVE (ψ_t^{RVE}) is defined in an analogous way to the microstructural twisting angle introduced in Section 4.1.3, and is calculated through a similar Procrustes analysis; the first input set of points is the fibre centres at the back section of the μCT-RVE ($x_{t,i,j=1}, y_{t,i,j=1}$), and the second set of points is obtained by adding the full-fibre displacement vectors ($\Delta u_{t,i}^{f}$, $\Delta v_{t,i}^{f}$). Analogous to the decomposition of fibre imperfection vectors into translational, twisting, and residual components in Section 4.1.3, the fibre displacement vectors were decomposed into kinking, torsional and residual components.

We also define the shear strain equivalent associated with the torsional motion($\gamma_t^{RVE,tors}$):

$$\gamma_t^{RVE,tors} = \frac{\psi_t^{RVE} R_{outer}^{RVE}}{L} \tag{16}$$

where R_{outer}^{RVE} is the equivalent radius of a cylinder with the same volume and length as the RVE.

5. μFEM with continuum elements and realistic fibre content

5.1. Assignment of fibre diameters

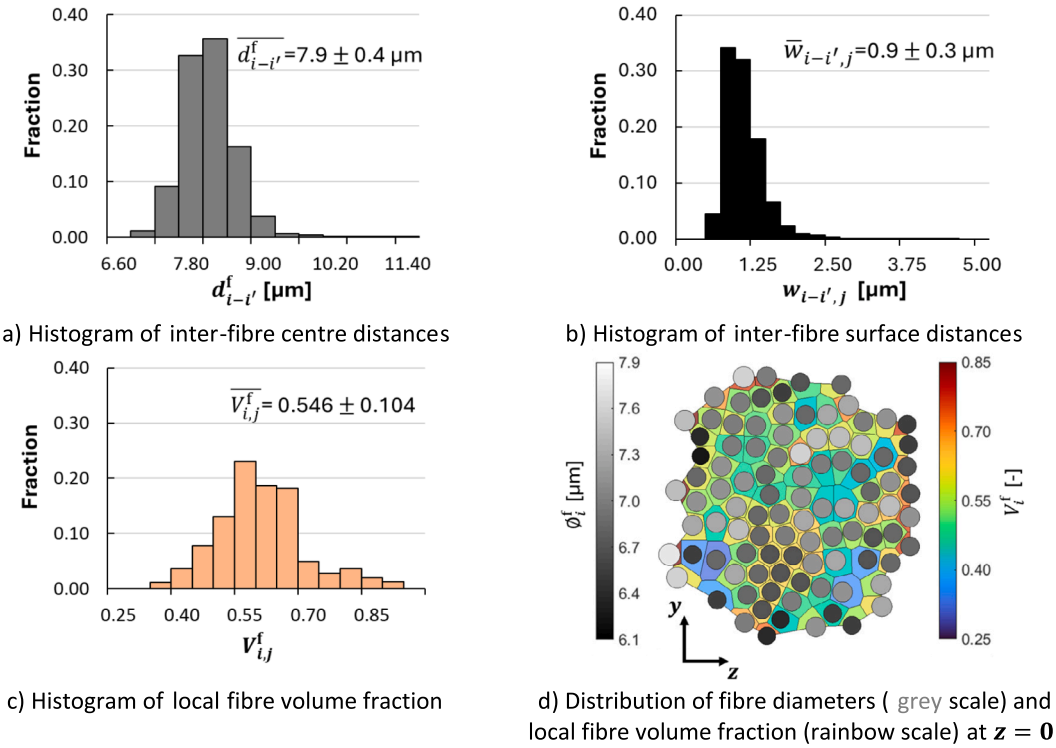
This section addresses the problem of avoiding interpenetration between neighbouring fibres. This problem is illustrated in Fig. 6a, which shows the histogram of inter-fibre-centre distances ($d_{i-i'j}^{f}$) for the μCT-RVE; this is calculated as the length of the alpha-triangulation edge between each fibre i and it neighbours i' in each j-section, as introduced in Section 2.2 and illustrated in Fig. 2. This means that $d_{i-i'j}^{f}$ includes the width of the matrix in between fibres i and i', as well as the fibre radii. Fig. 6a shows that approximately 1.2 % of the inter-fibre distances are smaller than the average fibre diameter ($\overline{\phi}^{f} = 7$μm in Table 1), with a minimum value of $\min\{d_{i-i'j}^{f}\} = 6.77$μm. Such cases prevent generating RVEs with a uniform fibre diameter equal to $\overline{\phi}^{f}$, as they lead to interpenetration of neighbouring fibres; the often-used solution [6,7,9] of artificially reducing the fibre diameter would lower the fibre volume fraction, which is also unsatisfactory.

To overcome this problem, we propose generating a statistical distribution of fibre diameters (identified as ϕ_i^{f}) that simultaneously (i) fulfils the non-interpenetration condition:

$$w_{i-i'j} = d_{i-i'j}^{f} - \left(\frac{\phi_i^{f}}{2} + \frac{\phi_{i'}^{f}}{2}\right) > 0, \tag{17}$$

where $w_{i-i'j}$, is the inter-fibre-surface distance, and (ii) is physically realistic (in the absence of μCT measurements of fibre diameters). Any variation in diameter along the fibre length (z-direction) and the non-circularity of fibre cross-sections are neglected. Therefore, fibre diameters are assigned following an artificial normal distribution [25,26] with a mean equal to the original dataset's average ($\overline{\phi}^{f} = 7$μm in Table 1), and a standard deviation consistent with laser diffraction measurements on similar fibres (i.e., T700SC: std = 0.3 μm) [12].

This normal distribution of fibre diameters is assigned spatially to fulfil Eq. (17) according to the following steps:



a) Histogram of inter-fibre centre distances

b) Histogram of inter-fibre surface distances

c) Histogram of local fibre volume fraction

d) Distribution of fibre diameters (grey scale) and local fibre volume fraction (rainbow scale) at $z = 0$

Fig. 6. Fibre distribution statistics and spatial variability in the μCT-RVE with 98 fibres.

a. **Generate** deterministically a list of N^f fibre diameters that follow the normal distribution, then sort them in ascending order.
b. **Determine** the minimum inter-fibre distance along each fibre i, i.e. $d^f_i = \min\left\{d^f_{i-i',j}\right\}$.
c. **Sort** the fibre IDs in ascending order of d^f_i.
d. **Assign** the sorted fibre diameters to the sorted fibres IDs.
e. **Verify** the absence of interpenetrations through Eq. (17).

This process has successfully generated a μCT-RVE where all neighbouring inter-fibre distances fulfil Eq. (17), as shown by the histogram in Fig. 6b. The resulting assignment of fibre diameters (ϕ^f_i) in the μCT-RVE is illustrated in Fig. 6d, as well as the local fibre volume fraction ($V^f_{i,j}$, calculated using a Voronoi diagram as explained in Supplementary Material (Section 1.2), with histogram in Fig. 6c).

The local fibre volume fraction at the boundaries of the section (as shown in Fig. 6d) depends on the alpha triangulation chosen for the μCT-RVE (controlled by alpha-shape value). Regardless of this choice, without the fibres at the boundaries and the corresponding (trimmed) Voronoi cells, the average fibre volume fraction in the inner portion of the μCT-RVE is $\overline{V}^f_{\text{inner}} = 51.2\%$.

5.2. Generation of RVEs with different lateral boundaries (using continuum elements)

5.2.1. Nominal RVE with alpha-shape boundary

This section addresses the problem of avoiding resin-rich areas at the lateral boundary of a μCT-RVE, by using the alpha-shaped cross-sections illustrated in Fig. 2. The 3D fibre geometry (shown in Fig. 1b-c) were constructed using Abaqus' *sweep* tool, which extrudes circular profiles along the defined fibre centrelines [21]. The fibres were then embedded within a matrix volume generated as follows:

1. For each j-section in the μCT-RVE, the alpha-shape triangulation was generated (as explained in Section 2.1) using an alpha-shape value of $a = 10.69$ μm. The alpha-shape value controls the cross-sectional shape of the RVE, and needs to be selected though trial-and-error: smaller values produce more concave cross-sections, thus avoiding resin-rich regions at the boundaries but potentially leading to severe discontinuities between consecutive sections, which can hinder the generation and meshing of a 3D volume; larger values yield more convex and more uniformity between consecutive sections, making it easier to generate and mesh a 3D volume, but leading to more resin-rich regions.
2. The geometric centre of each j alpha-shape was computed, to define a centreline for the μCT-RVE along the $z-$ axis.
3. Using Abaqus' *Loft* tool [21], a 3D irregular-shaped volume was created by connecting the N_z alpha-boundaries along the RVE centreline.
4. The alpha-shaped volume was then merged with the 3D fibres (using Abaqus's function *InstanceFromBooleanMerge* [21], partitioning the fibres and matrix), as shown in Fig. 3a.
5. The merged volume was then partitioned at each j-section.

The resulting alpha-shaped RVE meshed with continuum elements (CC-RVE) is shown in Fig. 7a. Its fibre volume fraction $V^f_{\text{CAE}} = 54.81\%$ is similar to that observed in the overall original dataset (in Table 1) [10], thus validating the selected alpha-shaped value ($a = 10.69$ μm).

5.2.2. Alternative RVEs

To investigate how the cross-sectional shape and matrix-rich regions on the lateral boundary affect the μCT-RVE response, two alternative CC-RVEs were generated using similar steps as outlined in Section 5.2.1, but modifying the shape of the j-sections as follows:

- Generating *convex-hull* j-sections in Step 1, as illustrated in Fig. 7b (corresponding to $a \to \infty$);
- Generating a *circular*-cylindrical volume enclosing all fibres instead of Steps 1–3 (as often done in the literature [6,9]), which leads to resin-rich regions near the lateral circular boundary.

An modified CC-RVE was generated using the same circular RVE boundary as in Fig. 7c, but with uniform fibre diameters; to prevent fibre interpenetration, the fibre diameter was reduced from 7 μm to 6.6 μm (consistent with previous studies [6,9]). The resulting fibre volume fraction of all CC-RVEs is shown in Table 3.

5.3. Mesh and model parameters

All CC-RVE models discussed in Section 5.2 were meshed using 10-node quadratic tetrahedral elements (C3D10), using a global seed of 2.5 μm. Table 3 summarises their geometrical and mesh parameters. The difference in element count between CC-RVEs with alpha-shape and convex-hull boundary is primarily because the latter required a more refined mesh "*curvature control*" in Abaqus CAE [21], to better capture the geometry of fibres with small inter-fibre distance near the RVE boundary (as highlighted in Fig. 7b).

All simulations in this study (unless stated otherwise) were carried out on Abaqus/Standard 2023, employing the Static Riks implicit, on a high-performance computer (HPC) equipped with a maximum of 80 cores and 750 GB of RAM, using an AMD EPYC 7742 server [27].

5.4. Baseline results of μFE-simulation of the alpha-shaped CC-RVE

Fig. 8 presents the global response of the alpha-shape μCT-RVE and reveals the following trends:

1. **At and immediately after X_c^{RVE} ("●" in Fig. 8), the results show that:**
   a. The predicted compressive strength is $X_c^{RVE} = 705.9$ MPa (see Fig. 8a), 21 % lower than experimentally measured for the same material [10] ($X_{c,exp}^{RVE}$ shown in Table 1). However, no conclusive argument can be extracted regarding the accuracy of the CC-RVE, as the selected volume may not be statistically representative of the overall microstructure.
   b. The kinking shear strain ($\gamma^{RVE,kink}$ in Fig. 8c) increases significantly, as expected for compressive failure due to kink-band initiation.
   c. The instantaneous kinking phase ($\varphi_{t,inst}^{RVE}$ in Fig. 8b) shows a distinct change in slope, indicating a change in the kinking direction.
   d. The torsional deformation (in Fig. 8d) also increases significantly; the magnitude of the torsional shear strain ($\gamma^{RVE,tors}$) is similar to the kinking shear strain, indicating the potential significance of torsion in the compression failure process.
2. **After X_c^{RVE} and up to $\varepsilon_{zz}^{RVE} = 0.85\%$ ("▲" in Fig. 8), the results show that:**
   a. The torsional angle reaches its maximum ($\psi_t^{RVE} = 16.5^\circ$ in Fig. 8d); this corresponds to an inflection point in all other curves in Fig. 8.
   b. This inflection suggests that the torsional deformation was contributing significantly to the stress drop in Fig. 8a.
   c. This inflection also suggests that the torsional deformation was exacerbating the magnitude of overall kinking (in Fig. 8c) and influencing the kinking direction (i.e. $\varphi_{t,inst}^{RVE}$ in Fig. 8b). This will be further discussed in the analysis of matrix yielding in Fig. 9.
3. **After the peak in torsional deformation (between "▲" and "×" in Fig. 8), the results show that:**
   a. The direction of torsional deformation reverses (i.e. the torsional angle decreases), and for the first time $\gamma^{RVE,kink} > \gamma^{RVE,tors}$ (Figs. 8c, d).
   b. This is followed by a rapid decrease in stresses (see Fig. 8a) which coincides with a rapid increase in $\varphi_{t,inst}^{RVE}$ and rapid increase of θ_t^{RVE} (see Figs. 8b,c). This phenomenon suggests excessive matrix yielding and lack of matrix support, allowing the RVE to kink significantly.

Fig. 9 illustrates the fibre displacements and plastic equivalent matrix strain for the CC-RVE with an alpha-shape boundary at the two

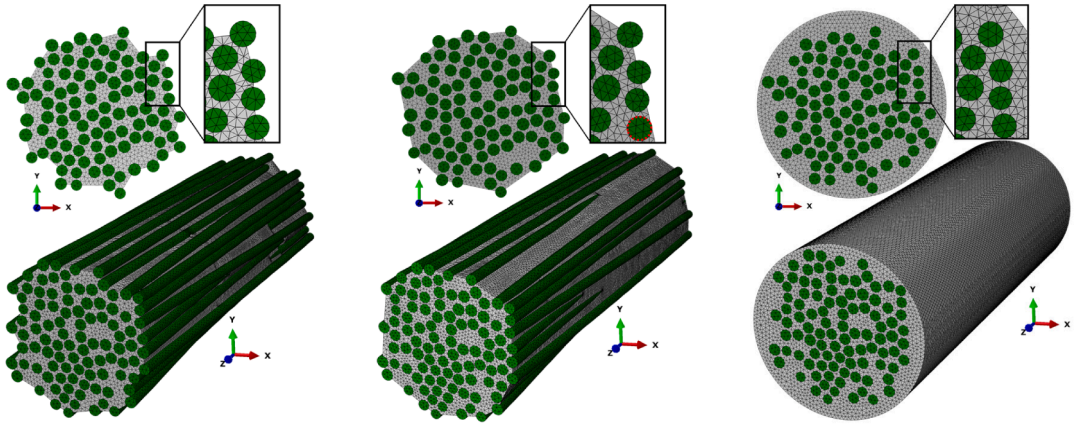


Fig. 7. Isometric and front-end view (from the positive z-axis) of the RVEs with different boundaries (with continuum elements). The zoomed-in images next to each RVE show the mesh in a location where neighbouring fibres exhibit small inter-fibre distance. The fibre marked in red in image b is discussed in Section 5.3.

Table 3
Global geometrical and mesh parameters for RVEs with continuum elements (CC). V_{CAE}^{f} is the fibre volume fraction as obtained from the "*mass properties*" tool in Abaqus.

	alpha-shape RVE	convex-hull RVE	circular RVE and ϕ_i^f distribution	circular RVE and uniform ϕ^f
Mesh curvature control	0.1	0.08	0.1	0.1
No. elements	2,014,643	2,507,862	2,601,344	2,779,870
No. distorted elements	1,271	1,109	20	58
Cross-sectional matrix area [μm^2]	3,116.18	3,381.02	6,429.19	6,796.84
V_{CAE}^{f}[%]	54.81	52.79	36.95	31.72

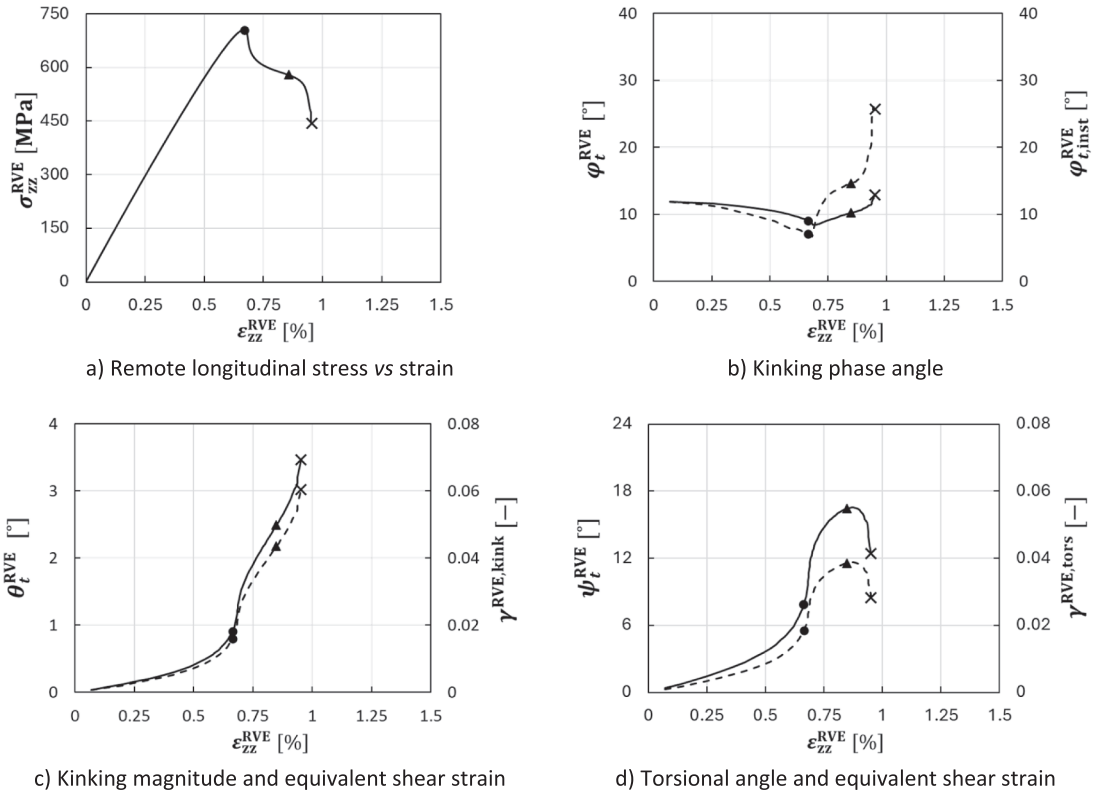


Fig. 8. Overall response of the CC-RVE with alpha-shape boundary. The solid (–) and dotted (–) lines on images (b)-(d) represent measurements in the left and right axis respectively. The "●" and "▲" markers correspond to the fields illustrated in Fig. 9b. The "×" marker corresponds to the first fully-failed fibre (with all integration points across a section fulfilling $\varepsilon^{f}_{11} < -\varepsilon^{f}_{11,X^{t}_{c}}$).

characteristic increments denoted with "●" and "▲" in Fig. 8. Fig. 9 reveals the following trends:

I. **Initially, at an increment corresponding to X_c^{RVE},** yielding occurs primarily at the positive *x*-boundary region of the RVE (Fig. 9b), where higher misalignment angles are present, including the most misaligned fibre of the RVE (as shown in Fig. 4a). Based on the longitudinal section view, yielding occurs nearly throughout the entire length of the RVE.

II. **Progressing to $\varepsilon_{zz}^{RVE} = 0.85\%$,** matrix yielding localises in bands running radially from a *x*-negative point near the cross-section boundary (Fig. 9b), and high $\varepsilon_{eq,p}^{m,CC}$ values are localised in the central region (near $z \approx 0$) of the RVE, indicating fibre kinking.

III. **Lastly, when comparing results at X_c^{RVE} vs. at $\varepsilon_{zz}^{RVE} = 0.85$, the trends reveal that:**

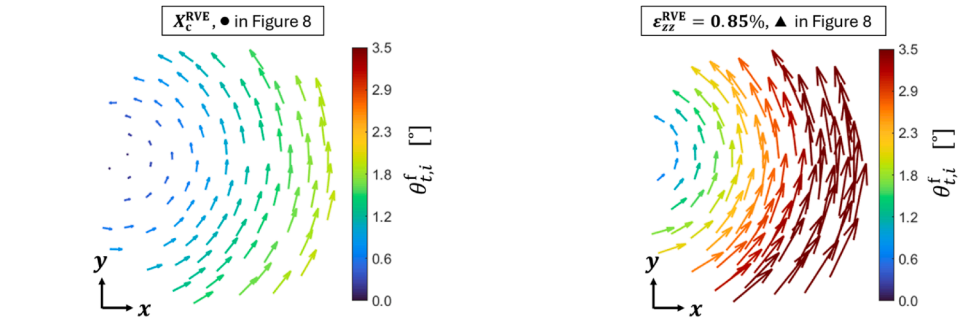
   a. There is a coordinated kinking and torsional deformation of the entire RVE (Fig. 9a).
   b. Regions with yielded matrix coincide with areas of elevated kinking magnitudes (~1.8° in Fig. 9a at X_c^{RVE}), showing that severe fibre kinking coincides with matrix yielding.
   c. The evolution of the locations of matrix yielding, as well as the radial yield-band patterns of $\varepsilon_{p,eq}^{m}$ fields, is aligned with the global RVE torsion suggested by Fig. 9a.

5.5. Effect of cross-section shape

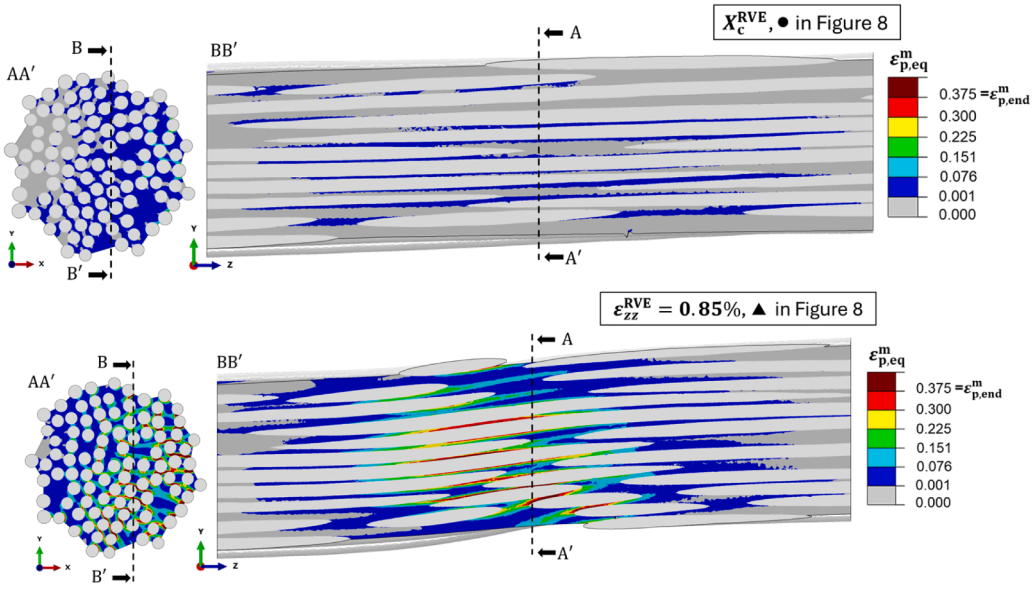
To investigate the effect of cross-sectional shape on composite's compressive performance, μFE simulations results of CC-RVEs with alpha-shape, convex-hull, and circular boundaries are presented in Fig. 10, and reveal the following mechanisms:

1. All CC-RVEs have similar stiffness in the force–displacement plot of Fig. 10a, as expected since the fibres are the primary load-bearing components. However, in the circular CC-RVE, matrix-rich boundary regions reduce the fibre content and consequently lower the apparent Young's modulus in the stress–strain response;
2. Although the fibre imperfections are the same across the CC-RVEs, differences in boundary matrix content significantly affect the maximum force (Fig. 10a); this is likely due to a significant increase in bending and torsional rigidity with increasing matrix content, as supported by the torsion simulations in Supplementary Material (Section 1.5);
3. The stability of the kinking phase angle throughout the entire loading history (φ_t^{RVE} in Fig. 10c) is positively correlated with the torsional rigidity of the CC-RVE (both are maximum for the circular boundary, and minimum for the alpha-shape boundary). Similarly, although the initial RVE misalignment phase ($\varphi_0^{RVE} = 12.85°$) aligns well with the observed RVE kinking phase ($8.5° \leq \varphi_t^{RVE} \leq 16.5°$) in all cases (Fig. 10c), this alignment is also positively correlated with the RVE torsional rigidity. This suggests that the overall direction of kinking is mainly governed by the preferential initial RVE misalignment direction, but also influenced by the torsional rigidity;
4. The hypothesised influence of cross-sectional geometry on bending/torsional rigidity from our previous study [9] is confirmed by the torsion angle trends in Fig. 10d (and validated by torsion μFE simulations, Supplementary Material, Section 1.5);
5. Compared to the alpha-shape CC-RVE, the resin-rich boundary regions in the circular CC-RVE reduce the torsion angle by a factor over 2 (Fig. 10d).

The cross-sectional shape, which influences both fibre kinking and torsion deformations, also affects the initiation and evolution of local matrix yielding, as shown by the correlation plots in Fig. 11. The trends



a) Fibre displacement vectors $\Delta_{t,i}^{f} = (u_{t,i}^{f}, v_{t}^{f})$ at front end of the RVE ($z = L/2$).



b) $\varepsilon_{eq,p}^{m}$ fields at the xy-section at $z = 0.0$ μm (AA', left) and yz- section at $x = 7.0$ μm (BB', right).

Fig. 9. Deformation of the alpha-shape CC-RVE, at two characteristic increments in $\sigma_{zz}^{RVE} - \varepsilon_{zz}^{RVE}$ in Fig. 8a. The colour maps in image a indicate the kinking magnitude angle as defined by Eq. (13) from the initial fibre centre (arrow base) to the displaced fibre centre (arrow tip) at the corresponding increment.

indicate:

- An overall higher degree of correlation in $\varepsilon_{eq,p}^{m,CC}$ is observed between the alpha-shape and convex-hull RVEs, particularly at X_c^{RVE} (Fig. 11a. iii). This is attributed to their similar matrix cross-sectional areas (see Table 3) and comparable fibre kinking behaviour (Fig. 10b-d). However, even small differences in fibre displacement can cause significant divergence in the $\varepsilon_{eq,p}^{m,CC}$ fields once deformation becomes severe (see Fig. 11b.iii);
- The circular-boundary RVE exhibits consistently weaker correlations with the other two CC-RVEs (Fig. 11, "i" and "ii").

The results in Fig. 10 and Fig. 11 indicate that μCT- RVE with a circular cross-section exhibits two critical limitations:

- It significantly underestimates the fibre volume fraction (by 29.1 %), leading to an unrealistic prediction of mechanical response (as shown in Fig. 10a);
- The artificially regular cross-sectional shape alters the torsional stiffness, thereby affecting both the global kinking and torsion deformations (see Fig. 10a-c) and the localisation of matrix yielding (see rows "i" and "ii" in Fig. 11).

In contrast, the μCT-RVE with an alpha-shape boundary produces a microstructure with a smaller cross-sectional area, reducing the total number of elements needed by at least 40 % (Table 3). This allows simulations of RVEs twice as large for the same computational time, partially mitigating edge effects associated with smaller RVEs.

5.6. *Effect of fibre diameter*

To assess the impact of using a realistic fibre diameter distribution versus a uniform diameter, CC-RVEs with circular cross-sections but different diameter distributions were compared, with key results summarised in Fig. 12. Based on Fig. 12a, notable differences in the composite's stress–strain behaviour are observed between the two cases, primarily due to differences in fibre volume fraction ($V_{CAE,const_\varnothing^f}^{f} = 31.72\%$ vs. $V_{CAE,vary_\varnothing^f}^{f} = 36.95\%$). In contrast, no significant difference is observed in the kinking phase (φ_t^{RVE} in Fig. 12b). This supports the hypothesis made in Section 5.5 (observation 3) that the kinking direction is primarily influenced by the mean misalignment phase angle of the misalignments in the microstructure, and secondarily by the torsional rigidity of the RVE.

The correlation plots of $\varepsilon_{eq,p}^{m}$ in Fig. 13 indicate a mostly consistent response of the CC-RVEs irrespective of fibre-diameter distributions, but with discrepancies attributed to two phenomena:

1. Differences in the fibre volume fractions (due to the reduction of the average diameter from 7 μm to 6.6 μm), which alters the overall rigidity of the RVE.

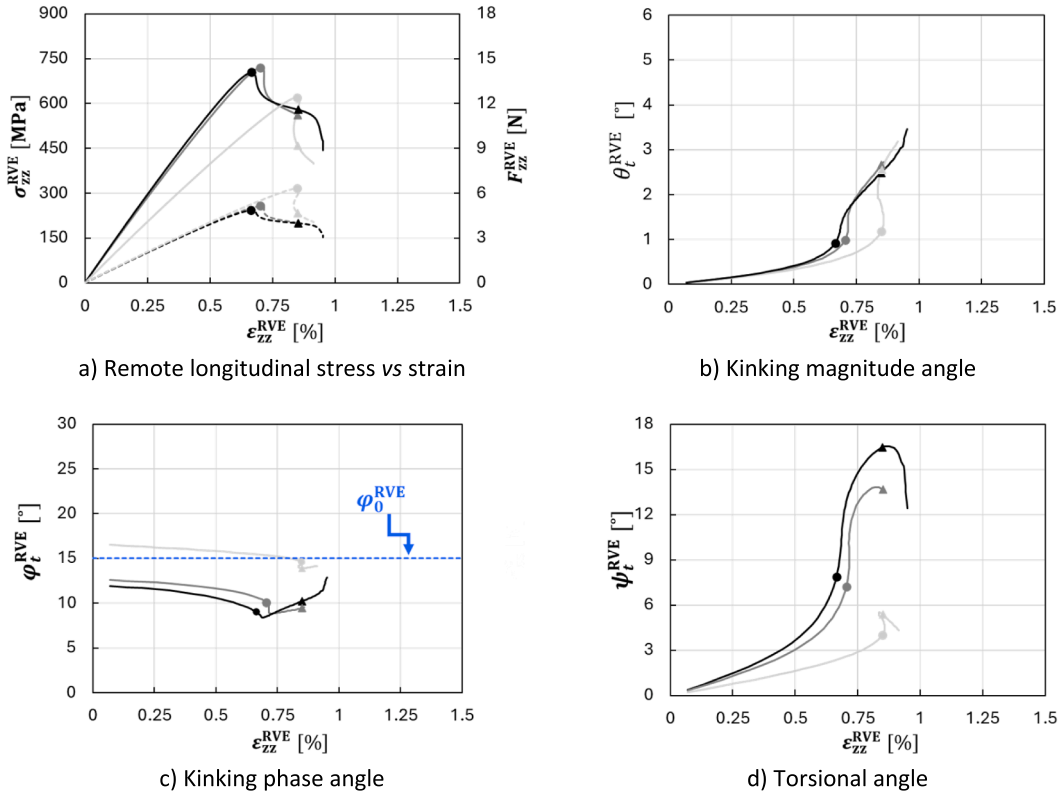


Fig. 10. Overall response of CC-RVEs with alpha-shape (black lines), convex-hull (dark-grey lines), and circular (light-grey lines) cross-sectional shapes. The solid (–) and dotted (–) lines on image (a) represent measurements in the left and right axis respectively. The "●" and "▲" markers correspond to the fields illustrated in Fig. 11. The dashed line in Subfigure (c) indicates the initial RVE misalignment phase.

2. Differences in inter-fibre spacing caused by the diameter distribution, which affects the initiation and evolution of matrix yielding (delayed in the CC-RVE with uniform fibre diameters, due to the larger average inter-fibre-surface distance / matrix width).

However, as these two phenomena are closely interlinked, the main cause of the discrepancies seen in Fig. 12 and Fig. 13 is debatable. In any case, accounting for a realistic fibre diameter distribution is essential for accurately simulating the RVE's true inter-fibre spacing distribution and true fibre content.

6. Computationally efficient μFEM

The computationally-efficient Shell-Beam (SB) micromechanical FE-methodology initially introduced in our previous work [9] is employed in this section and compared to the CC-RVE counterpart with alpha-shape boundary (proposed for the first time in Section 5.5). Since the SB- and CC-RVEs are based on the same cross-sectional alpha-shapes, this comparison minimises discrepancies in the μCT-RVE response that would appear with a circular CC-RVE; such discrepancies were a limitation in our previous work [10], as suggested in Section 1, and corroborated by the significant effects of cross-sectional shape shown in Section 5.5.

6.1. Overview of the SB μFEM

6.1.1. SB variations and RVE generation

The two Shell-Beam (SB) formulations, SB_s (Shell-Beam variation with sharing nodes) and SB_k (Shell-Beam variation with kinematic links) are illustrated in Fig. 14, and consist of the following elements:

- **Linear Timoshenko beam elements (B31)** are used to model the imperfect paths of each individual fibre [9] using the fibre centre coordinates defined in Section 2. A circular beam cross-section is defined, with a fibre diameter (ϕ_i^f) that follows the distribution shown in Fig. 6d and assigned as described in Section 5.1. The fibre's constitutive properties used for both SB variations are identical to the CC-RVE counterpart, as described in Section 3.1.
- **4-node linear shell elements (S4R)** are used to model the matrix between neighbouring fibres [9], placed based on alpha-shape triangulations, as shown in Fig. 2 (and Fig. 14).
  - o **In the SB_s**: shell elements are positioned between the centrelines of neighbouring fibres and share nodes with the adjacent beam elements, matching the triangulation edges shown in Fig. 6 and illustrated in Fig. 14a.
  - o **In the SB_k**: shell elements do not share the nodes with beam elements. Instead, they reflect the actual matrix width between fibres. Kinematic links are employed to couple the fibre and matrix elements in this variation, as shown in Fig. 14b.

6.1.2. Calibration of matrix constitutive shear strains

The matrix material model used in the shell elements must be calibrated from the constitutive shear response (defined in Section 3.1) to account for the discrete nature of the shell elements connecting neighbouring fibres. This calibration process was proposed and explained in our previous work [9]; while the calibration of equivalent stresses remains unchanged, we have improved the calibration of strains (which is required only for the SB_s variation), as we describe below. The full details and governing equations required to calibrate the matrix yield stresses, yield strains, and elastic constants are provided in the Supplementary Material (Section 1.2). Supplementary Material also contains the resulting Abaqus inputs of the calibrated properties of the matrix used in the SB-RVEs, along with the uncalibrated properties for the CC-

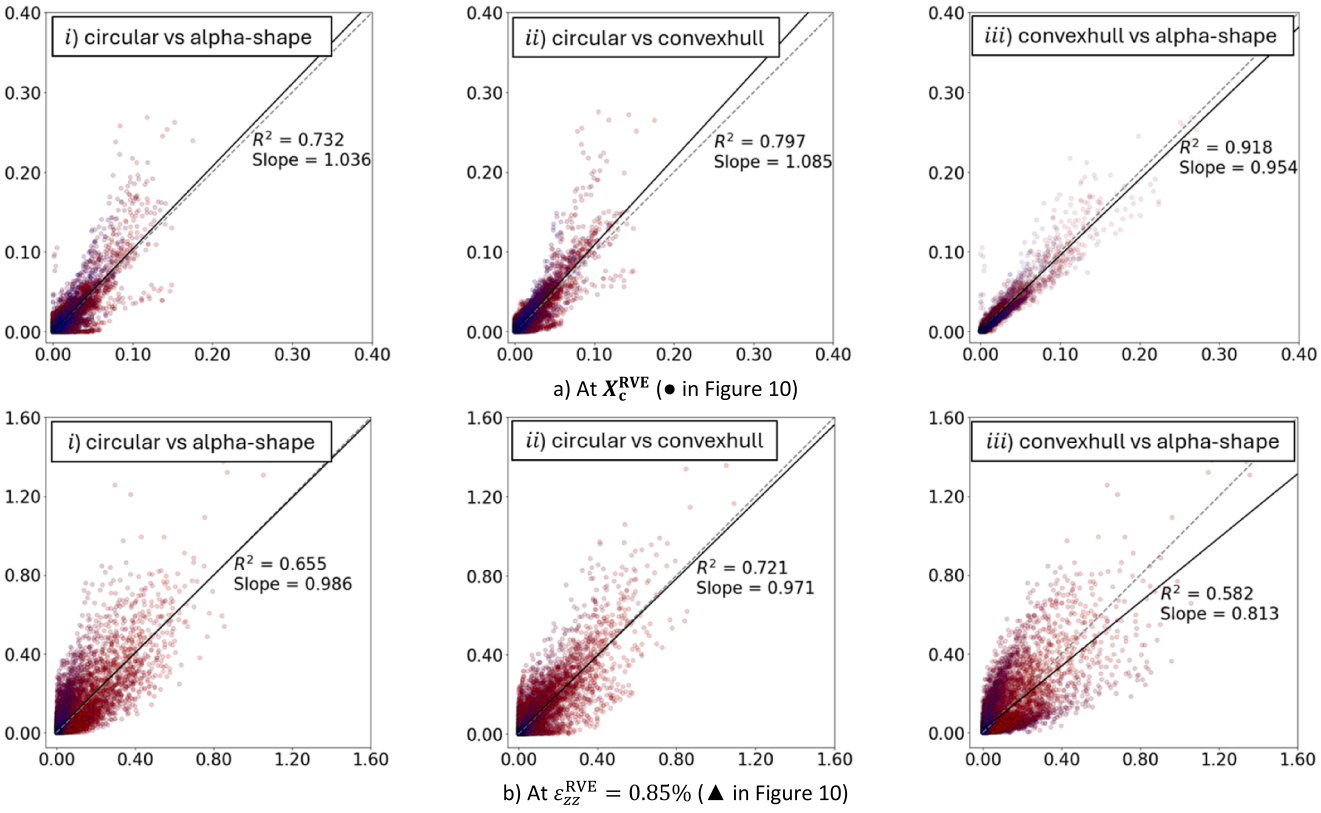


Fig. 11. $\varepsilon_{eq,p}^{m,CC}$ correlation plots among the CC-RVEs with different cross-sectional shapes, for the two characteristic increments defined in Fig. 10. The scatter is colour-coded according to their distance ($|z|$) from the mid-plane ($z = 0$), where red-coloured points suggest locations near the central region of the RVE 0 $L/2$. The solid black regression line quantifies the correlation, while the dotted (–) grey line represents a one-to-one agreement (y = x).

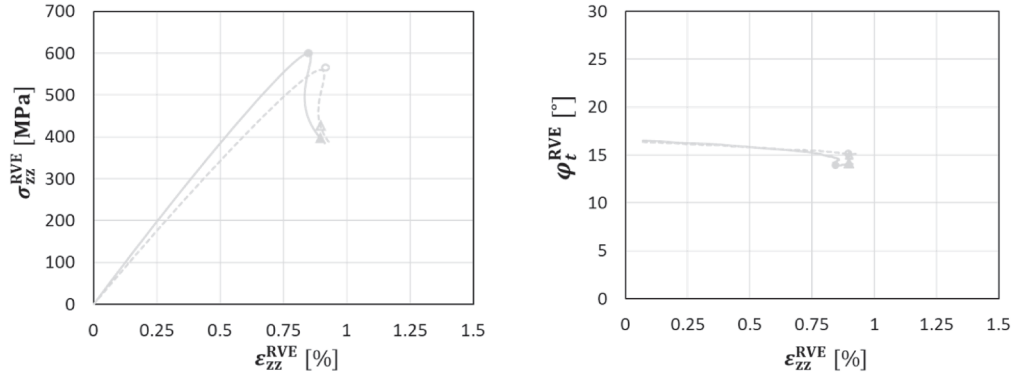


Fig. 12. Overall response of the alpha-shape CC-RVEs with varying (continuous " –" lines, filled markers "●▲") and uniform (dotted " – –" lines, open markers "○△")) fibre diameters. The markers correspond to the fields illustrated in Fig. 13.

RVEs.

Based on our previous work [9], the calibrated matrix shear strains for the SB_s variation, $\gamma^{m,SBs}$, are linked to the uncalibrated constitutive shear strains, $\gamma^{m,CC}$, through a strain independent calibration factor $K_\varepsilon^{SB_s}$, as follows:

$$\gamma^{m,SBs} = K_\varepsilon^{SB_s} \cdot \gamma^{m,CC}. \tag{18}$$

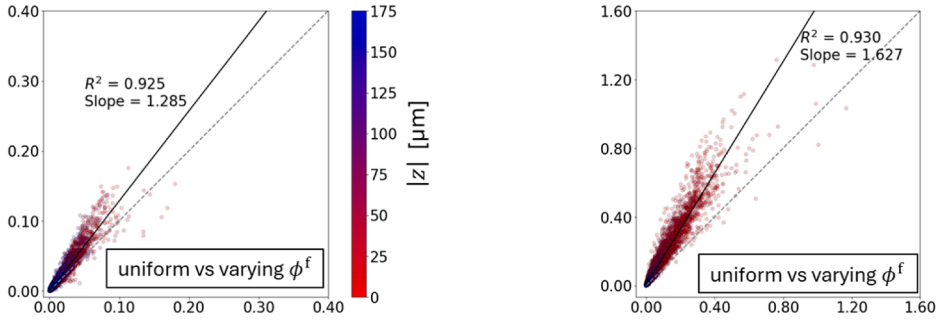
In our previous work, $K_\varepsilon^{SB_s}$ was defined as

$$K_\varepsilon^{SB_s} = \frac{\gamma^{m,SBs}}{\gamma^{m,CC}} = \frac{1}{1 + \frac{\phi^f}{W_{hex}^{UC}}} = 1 - V^{f(2D)}, \tag{19}$$

where $V^{f(2D)}$ is the fibre volume fraction in a 2D layered composite with the same inter-fibre-surface distance (or matrix width) as in a composite with hexagonal packing [28]. However, based on Chamis's modified rule of mixtures [29], the right-hand side of Eq. (19) can alternatively be expressed as:

$$K_\varepsilon^{SB_s} = 1 - \sqrt{V^f}\left(1 - \frac{\overline{G}^{m,cc}}{G_{12}^f}\right), \tag{20}$$

where $\overline{G}^{m,cc}$ is the secant shear modulus of the constitutive matrix response. Assuming shear-rigid fibres, as in many micromechanical models [15], this further simplifies to:



a) $\varepsilon_{eq,p}^{m,CC}$ plot at $\boldsymbol{X_c^{RVE}}$ (● in Figure 12)

b) $\varepsilon_{eq,p}^{m,CC}$ plot at $\varepsilon_{zz}^{RVE} = 0.90$ % (▲ in Figure 12)

Fig. 13. $\varepsilon_{eq,p}^{m,CC}$ correlation plots among the cc-rves with circular cross-section and with uniform and varying fibre diameter. The scatter is colour-coded according to their distance ($|z|$) from the mid-plane ($z = 0$), where red-coloured points suggest locations near the central region of the RVE 0 ——— $L/2$. The solid black regression line quantifies the correlation, while the dotted (–) grey line represents a one-to-one agreement (y = x).

$$K_{\varepsilon}^{SB_s} = 1 - \sqrt{V^f}. \tag{21}$$

Preliminary μFE simulations (not shown here) have demonstrated results of improved accuracy using Eq. (21) compared to the original expression (Eq. (19)) used in our previous work [9]. Therefore, Eq. (21) is adopted in the present paper to calibrate the matrix shear strains for the SB_s model.

6.1.3. Boundary conditions

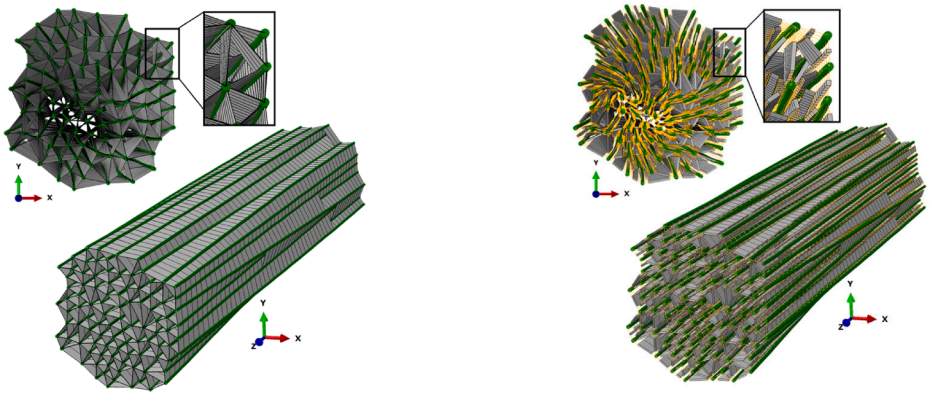
For both SB model formulations, the boundary conditions described in Section 3.2 are applied to the fibre nodes at the end sections of the RVE ($z = -L/2$ and $z = L/2$). In addition, the bending rotations of the fibre nodes at these end sections are constrained, i.e. $\{v_r, w_r\}(z = \{z = -L/2, z = L/2\}) = 0$, to ensure kinematics consistency between the SB-RVEs and the CC-RVEs (as such rotations are implicitly restricted by the uniform longitudinal displacement boundary conditions in the latter).

For the SB_k formulation, kinematic coupling constraints are applied to connect each fibre node to its corresponding neighbouring matrix nodes, as shown in Fig. 14b. In Abaqus, this is realised using the **kinematic coupling* keyword [21], where all degrees of freedom – both translational and rotational – of the *secondary* matrix nodes are coupled to the corresponding fibre *main* node (i.e. each coupling behaves as a rigid beam).

6.2. SB validation against CC-RVEs

Fig. 15 summarises the global response for the CC–, SB_k-, and SB_s-RVEs. The comparison across the different FE methodologies reveals the following:

1. **On one hand, there is an excellent agreement among the RVEs in terms of:**
   a. The initial stiffness (maximum error CC vs. SB_s: 0.36 %) and compressive strength (maximum error CC vs. SB_s: 13.41 %), as shown by Fig. 15a, which is aligned with previous comparisons between CC and SB models [9];
   b. The kinking phase (Fig. 15b) and kinking magnitude (Fig. 15c) throughout the compression simulation. This constitutes an improvement over previous results [9], confirming that these metrics are highly sensitive to the RVE's cross-sectional shape and torsional rigidity;
2. **On the other hand, larger differences among the RVEs are observed in terms of:**
   a. The shape of the $\sigma_{zz}^{RVE} - \varepsilon_{zz}^{RVE}$ curve after X_c^{RVE}, where CC-RVE has more pronounced changes in $\sigma_{zz}^{RVE} - \varepsilon_{zz}^{RVE}$ slopes compared to the



a) SB_s formulation

b) SB_k formulation

Fig. 14. Isometric and front-end views of the SB- RVEs. The triangulation network used to generate the shell elements is based on the alpha-shape with $a = 10.69$ μm, resulting into a geometry directly equivalent to the CC-RVE with alpha-shape boundary (Fig. 7a). The two SB formulations are visualised accounting for the shell thickness (scaled by a factor of "0.2") and the fibre radius (scaled by a factor of "0.3").

SB cases. As discussed in Section 5.4 (observations 2b-2c), differences in the shape of $\sigma_{zz}^{RVE} - \varepsilon_{zz}^{RVE}$ are potentially associated with the difference in torsion angles, ψ_t^{RVE} (see Fig. 15d), which are also expected to affect the evolution of matrix yielding.

b. The torsion angles (Fig. 15d), which are higher for the CC-RVE case compared to the SB counterparts (with a maximum of 31.5 % difference when comparing CC vs. SB_s). This difference arises from variations in matrix content: SB models include a boundary matrix layer defined by the shell element thickness, resulting in a slightly different matrix volume compared to the CC model. The larger discrepancy between SB_s and the other cases likely stems from the calibration process and the altered stress-component contributions under compression in the SB_s formulation, specifically $G^{m,SB_s} \approx G^{m,CC} K_\sigma^{SB_s} / K_\varepsilon^{SB_s}$ and $E^{m,SB_s} = E^{m,CC}$. This modification potentially limits the RVE's torsional deformation (as indicated by the difference torsional modulus in Supplementary Material among the cases) and leads to smaller torsional angles.

Fig. 16 illustrates correlation plots of $\varepsilon_{eq,p}^{m,CC}$ for the three FE methodologies (CC, SB_k, and SB_s), compared in pairs at two characteristic loading increments. The correlation plots reveal the following:

- There is excellent agreement between CC– and SB_k-RVEs at both increments. Despite differences in torsional behaviour (Fig. 15d), the $\varepsilon_{eq,p}^{m}$ fields are well aligned across the two models;
- For the same increment, the SB_s-RVE systematically predicts lower magnitudes of equivalent plastic strain compared to both CC– and SB_k-RVE. This is consistent with the calibration-related differences discussed in the same section (observation 2b), which may limit torsional motion and reduce values of $\varepsilon_{eq,p}^{m,CC}$. An additional contributing factor could be the increased (artificial) inter-fibre centre distance in the SB_s-RVE, which reduces the effective local fibre volume fraction and delays yielding, potentially affecting X_c^{RVE}.

Fig. 17a presents the $\varepsilon_{eq,p}^{m}$ fields at the mid-section of the RVE ($z = 0$) at X_c^{RVE}, for the CC–, SB_k- and SB_s-RVEs. Additionally, Fig. 17b overlays the $\varepsilon_{eq,p}^{m}$ histograms onto the matrix's constitutive response, also at X_c^{RVE}. The following observations are made:

- The locations where matrix yielding initiates (Fig. 17a) are consistent across all FE methodologies; however, the SB_s-RVE consistently underpredicts the magnitudes of equivalent plastic strains (as shown in Fig. 16), the CC– and SB_k-RVE show excellent agreement.
- The proportion of regions where the matrix is near its constitutive peak is significantly lower in the SB_s-RVE (0.11 %) than in the CC-RVE (1.28 %) and SB_k-RVE (1.92 %) (Fig. 17b). This discrepancy is also observed in unit cell simulations with hexagonal and square fibre packing, where the SB_s-UC and CC-UC share equivalent geometries [9].

Fig. 18 shows the $\varepsilon_{eq,p}^{m}$ fields on the mid- yz plane at the increment corresponding to the first fibre failure (defined in Fig. 15a), for the three FE methodologies. All cases show a full matrix-yield band across the width (y-direction) of the RVEs. The location and dimensions of the yield band are consistent across all FE methodologies, appearing in the central region of the specimen, with a width - $86 < z < 93$ μm, and an orientation $11 < \beta < 16^\circ$. These values are lower than typically reported in the literature for fully-formed kink-band (with widths often from 125 μm to 400 μm) and kink-band orientations of (approximately 30° [5,30]); this discrepancy is potentially explained by the small dimensions of the μCT-RVE.

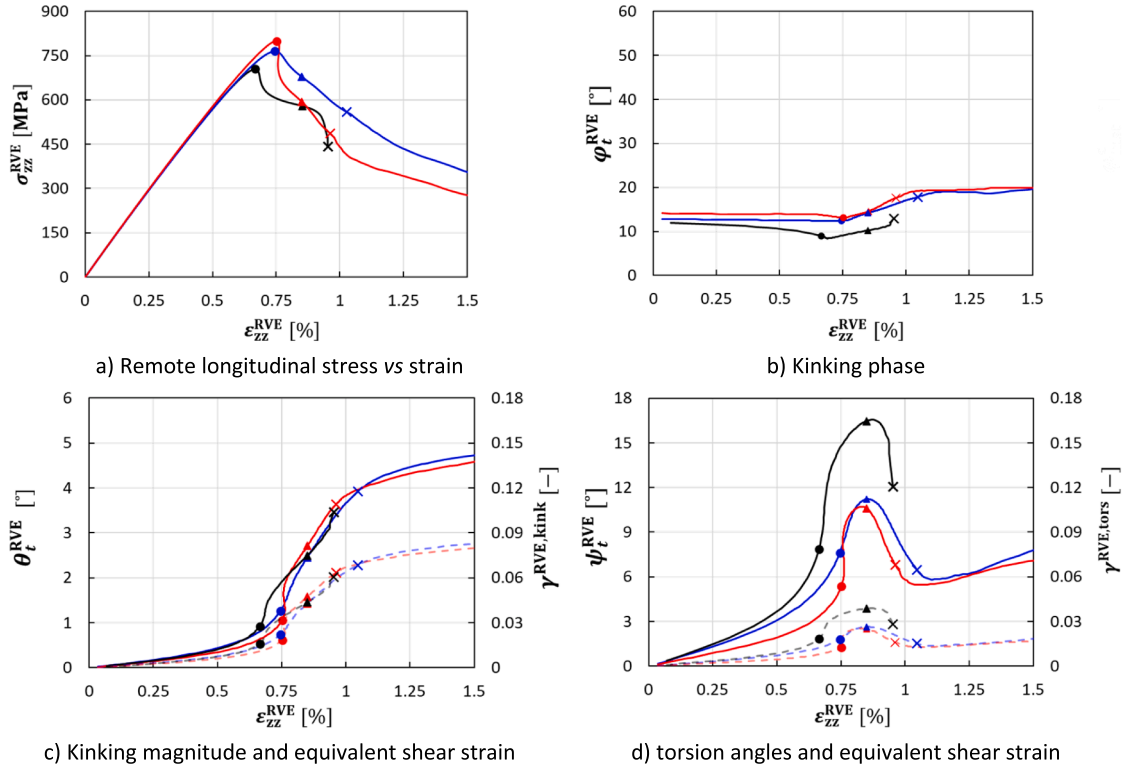


Fig. 15. Overall response of the alpha-shape CC (black lines), SB_k (blue lines), and SB_s (red lines) RVEs. The "●" and "▲" markers correspond to the fields illustrated in Figs. 16 and 17. The solid (–) and dotted (–) lines on images (c-d) represent measurements in the left and right axis respectively. The "×" marker corresponds to the first fully-failed fibre (with all integration points across a section fulfilling $\varepsilon_{11}^{f} < -\varepsilon_{11,X_c^f}^{f}$) and to the kink-band geometry shown in Fig. 18 (the CC simulations aborted after the first fibre was fully failed).

7. Discussion

7.1. Failure mechanisms during longitudinal compression

The comparative investigation presented in Sections 5 and 6 revealed novel microscopic mechanisms during longitudinal compression. These are summarised in Fig. 19 for the case of the SB_k-RVE (with alpha-shape boundary), which demonstrated excellent agreement with the CC-RVE and allowed the simulation to progress beyond the first fibre failure to the formation of a kink-band with edges fully defined by broken fibres, revealing the following sequence of events:

1. **Matrix yield initiation (Fig. 19a-c, "◆"), when the following happens:**
   a. Matrix yielding begins in isolated regions at the lateral boundary of the RVE;
   b. Fibres experience nearly-uniform compression as evidenced by a homogeneous stress field;
   c. The entire RVE undergoes coordinated deformation through torsion and kinking, with only a small component for the residual deformation of individual fibres, $\overline{\Delta_{t,i}^{\mathrm{f,res}}}$ (Fig. 19c).
2. **Remote peak stress (Fig. 19a-c, "■"), when the following happens:**
   a. Matrix yielding becomes widespread in the middle of the RVE, as shown in Fig. 19a;
   b. Bending strains develop in the fibres, peaking at the RVE ends (Fig. 19b);
   c. The RVE continues to deform in coordinated kinking and torsion modes. The equivalent shear strain due to torsion might reach a peak, while that due to kinking continues to increase monotonically (Fig. 19g). Again, there is a negligible residual component, $\overline{\Delta_{t,i}^{\mathrm{f,res}}}$ (Fig. 19c).
3. **Fibre failure initiation (Fig. 19a-c, "▲"), when the following happens:**
   a. A fully developed yield band appears in the matrix, as shown in Fig. 19b, with large plastic strains reaching or exceeding the end of the input constitutive law (i.e., $\varepsilon_{\mathrm{p,end}}^{\mathrm{m}}$ Fig. 3b). Beyond this point, the results should be interpreted with caution, as matrix cracking is likely to occur and may influence the subsequent failure response of the composite;
   b. The location of fibre bending shifts to inside the yield band, and fibre failure initiates near the lateral boundaries (see Fig. 19b);
   c. The coordinated torsional deformation of the μCT-RVE starts decreasing, while the coordinated kinking deformation mode continues growing significantly (Fig. 19c).
4. **Fibre failure propagation (Fig. 19a-c, "●"), when the following happens:**
   a. The matrix yield-band (Fig. 19a) exhibits extensive plastic deformation, with a large proportion of matrix reaching $\varepsilon_{\mathrm{p,end}}^{\mathrm{m}}$ (Fig. 3b). This is driven by intense shear due to fibre kinking and continued fibre failure;
   b. The kink-band boundaries (Fig. 19b) are fully formed as fibre failure propagates across the RVE's lateral surface (y-direction) and the through its core (x-direction);
   c. The coordinated torsional deformation of the RVE further diminishes (Fig. 19c and Fig. 19e). The coordinated kinking deformation of the RVE continues increasing in magnitude; however, as

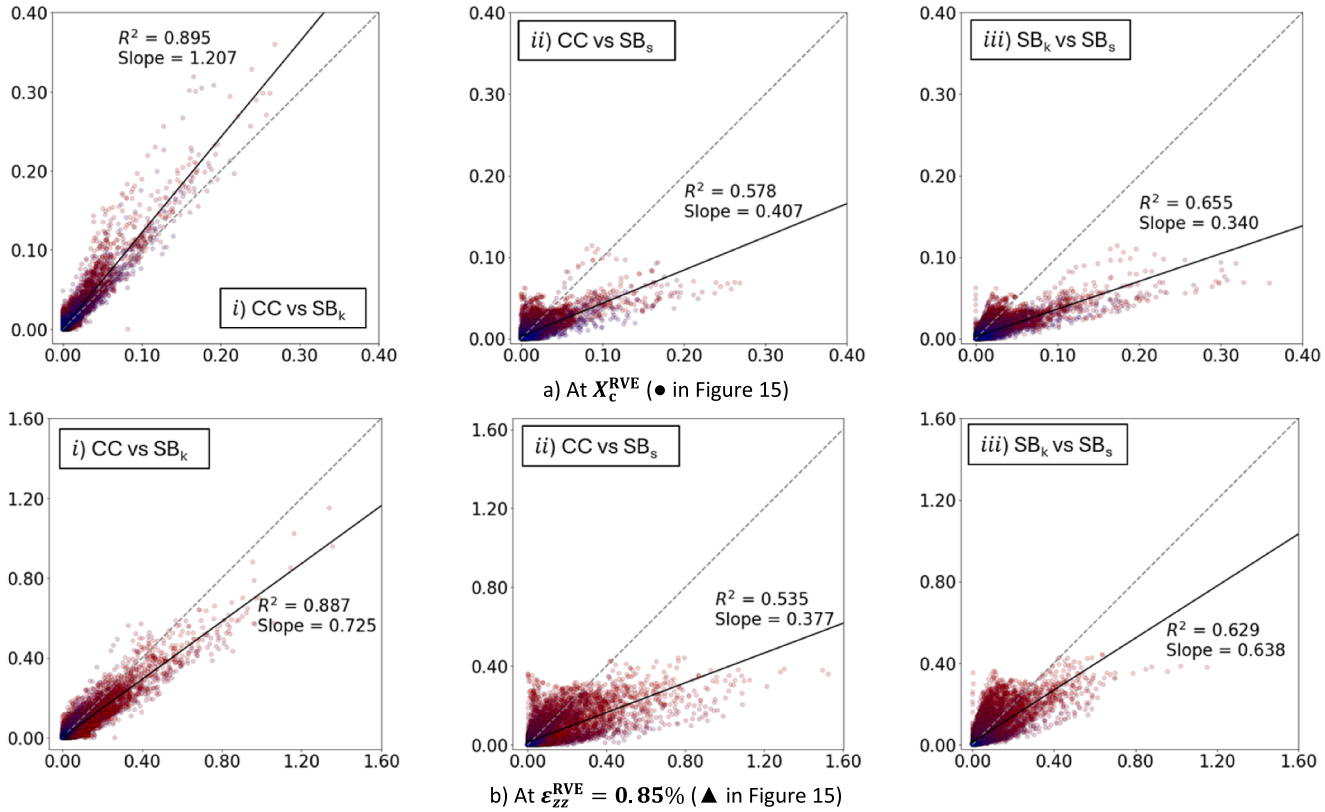


Fig. 16. $\varepsilon_{\mathrm{eq,p}}^{\mathrm{m}}$Correlation plots among cc–, SB_k-, and SB_s-RVEs with alpha-shape boundary. The scatter is colour-coded according to their distance ($|z|$) from the mid-plane ($z = 0$), where red-coloured points suggest locations near the central region of the RVE 0 $L/2$. The solid black regression line quantifies the correlation, while the dotted (–) grey line represents a one-to-one agreement (y = x).

shown in Fig. 15b, the kinking phase remains unstable and fluctuates.

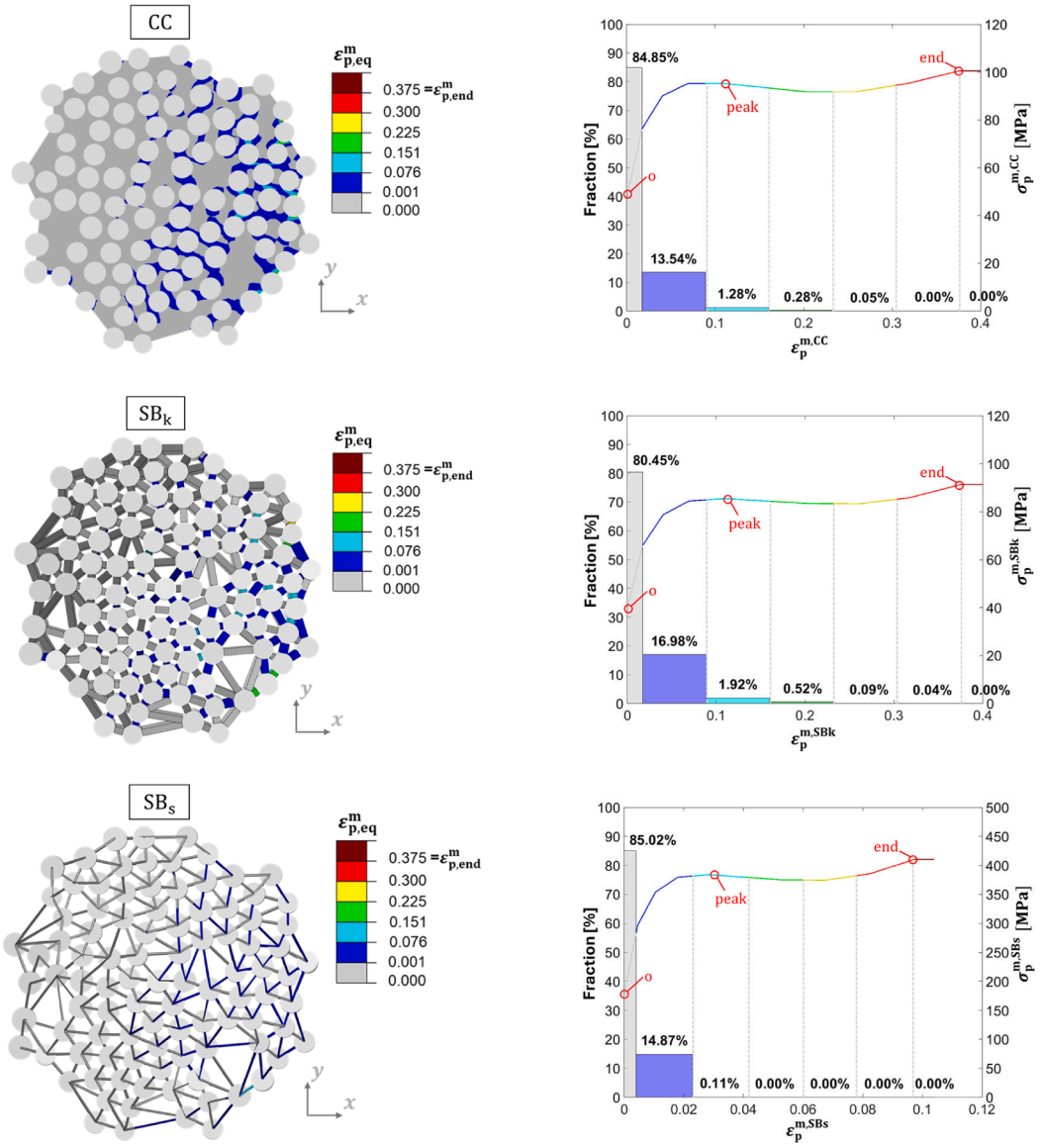
7.2. Limitations and opportunities

The comparison between the predictions from the CC– and SB-RVEs (Section 6) demonstrates the excellent accuracy of the SB_k models in capturing the compressive strength, RVE kinking and torsion deformation modes (Fig. 15), the evolution and location of matrix yielding (Fig. 17), and the matrix yield-band dimensions (Fig. 18). The strong correlation between the $\varepsilon^{m}_{eq,p}$ fields predicted by the SB_k- and CC-RVEs, shown by the histograms in Fig. 17 and correlation plots in Fig. 16, signifies the ability of the SB_k methodology to predict the microscale features and mechanisms involved in compressive failure. The accuracy of the SB_k methodology is further put into context through the correlation plots for matrix yielding strains among the CC-RVEs with different cross-sections (Fig. 11) and fibre diameter distributions (Fig. 13), which presented similar or even worse correlations.

Therefore, this paper confirms the predictive power of the SB methodology and establishes it as an efficient approach for investigating the effects of real fibre imperfections derived from μCT data. It advances our previous work [9] by ensuring geometric equivalence in cross-sectional shape between the CC and SB models. As demonstrated here, and consistent with earlier findings [9], matrix-rich boundary regions in μCT-RVEs can significantly obscure the effects of microstructural twisting and the coupling between compression and torsion, which have also been reported in much larger RVEs [1].

Nevertheless, the SB methodologies can be further improved, particularly regarding the calibration of the matrix constitutive law. The calibration required to match the shear response between CC– and SB-RVEs results in the development of inconsistent direct matrix stresses (especially for the SB_s variation), as discussed in our previous work [9]. Although this has a limited influence on matrix plasticity under the von Mises criterion used here, the effect may become more pronounced with a pressure-dependent constitutive law.

Future developments should therefore decouple the calibration of



a) $\boldsymbol{\varepsilon^{m}_{eq,p}}$ fields at section $\boldsymbol{z = 0}$ (constitutive values, as defined in Section 3.1.2)

b) Histogram of $\boldsymbol{\varepsilon^{m}_{eq,p}(x, y, z)}$ plotted on the plastic stress-strain curve of matrix

Fig. 17. $\varepsilon^{m}_{eq,p}$ for the CC–, SB_k-, and SB_s-RVEs, at X_c^{RVE}. The colour-coding is consistent across all plots.

shear from other stress components and incorporate additional mechanisms, such as pressure-dependent plasticity, matrix failure, and local variations in matrix behaviour arising from geometric confinement during curing and size effects in narrow inter-fibre regions [31,32]. Further developments should also include additional failure mechanisms, such as fibre–matrix debonding and splitting to more accurately capture the complex evolution of composite failure.

Recent parametric unit-cell simulations [15,33,34] have examined the influence of matrix constitutive plasticity parameters, such as dilation and friction angles, on composite performance. Supported by recent experimental evidence on dilation angle [34] and friction angle [15,33], these studies show that, within realistic parameter ranges, matrix pressure-dependent effects have only a secondary influence on compressive strength. Instead, the dominant contribution arises from fibre imperfections and their associated microstructural variability, reinforcing the central focus of the present study: capturing the effects of realistic fibre architectures and imperfections on the compressive response.

The SB-RVE methodology, combining accuracy and computational efficiency, opens several avenues for future research:

i. **Critical RVE size:** Determine the minimum RVE size under longitudinal loading (a topic extensively explored only for transverse loading) that ensures converged strength predictions and statistically representative fibre architectures of the overall UD ply;
ii. **Characterisation of critical imperfections:** Identify the key microstructural features that drive kink-band initiation and propagation, and relate them to the initial fibre architecture. As the current work highlights the coupling between fibre imperfections, RVE misalignment and twisting, and torsional and kinking deformation modes, future studies should aim to decouple these features and mechanisms and quantify their respective contributions to compressive response. Such analyses would benefit from synthetic yet statistically representative RVEs.
iii. **Bridging the length scales**: Explicitly model critical microstructural regions within otherwise homogenised domains that also account for the influence of adjacent plies in a laminate. This multiscale approach would enable a more accurate connection between the micro- and *meso*-scales, and also improve the understanding of the coupled kinking–torsion mechanisms (as recently evidenced in the literature [1]) at larger or even laminate-level scales. As these mechanisms are inherently 3D, bridging the length-scales requires fully 3D modelling to capture their complex interactions, making the SB-μFEM ideally suited for such investigations.
iv. **SB validation**: Conduct direct validation against compression experiments of UD-FRPs with well-characterised constituent and microstructures. Leveraging on its computational efficiency, the SB methodology could be benchmarked against full μCT-scanned volumes and *in-situ* experimental data (e.g., [1]), providing a robust and verified methodology for testing and interpreting hypotheses from in-situ experimental observations.

8. Conclusions

This is the first study that addresses the following three challenges in μFE simulations of real FRPs microstructures obtained from μCT data:

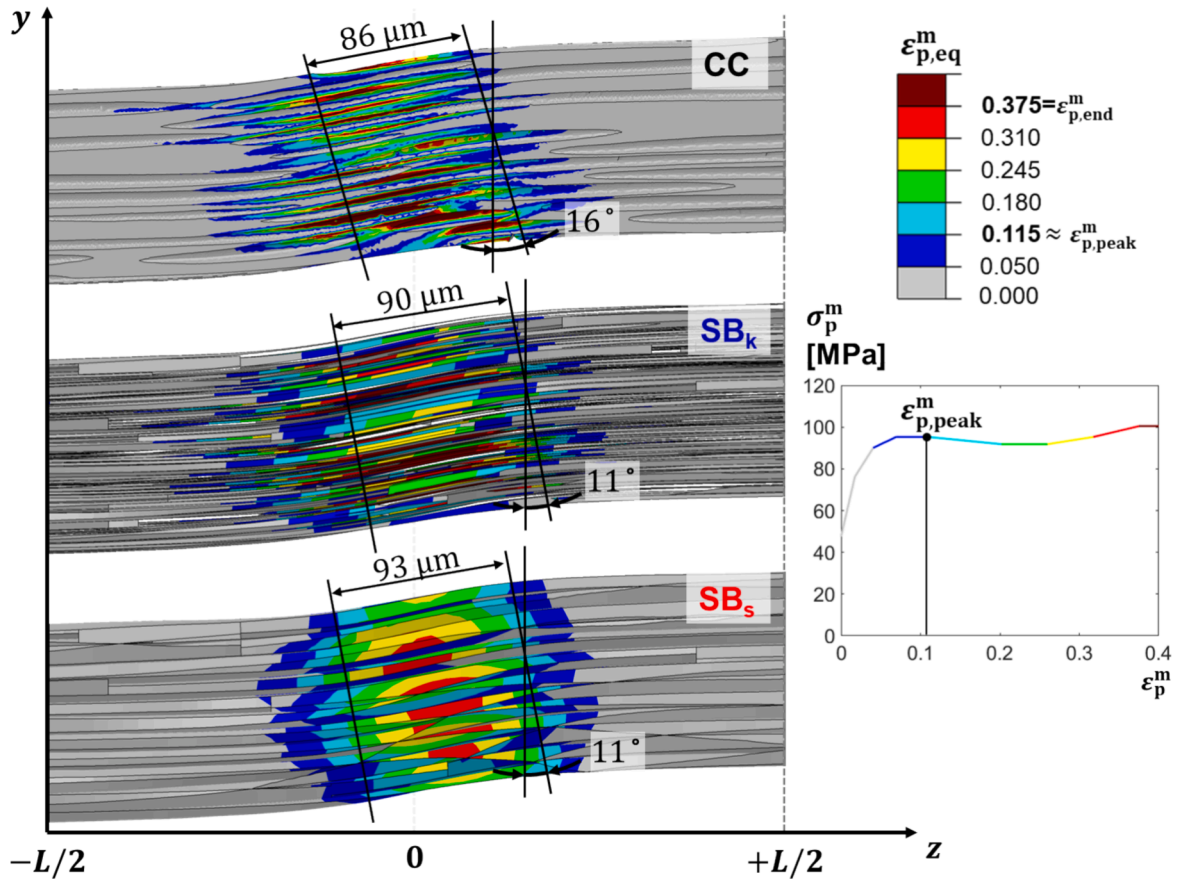


Fig. 18. $\varepsilon^{m}_{p,eq}$Fields for cc–, SB_k-, SB_s-RVEs with alpha-shape boundary on a longitudinal section ($x = 0$). The fields are obtained at the increment corresponding to the fibre failure initiation (defined in Fig. 15). The illustrated kink-band is defined as the narrowest band with straight ends satisfying the condition $\varepsilon^{m}_{p}(x = 0) > \varepsilon^{m}_{p,peak}$ at least one integration point of all elements, with width and β-angle shown for each case.

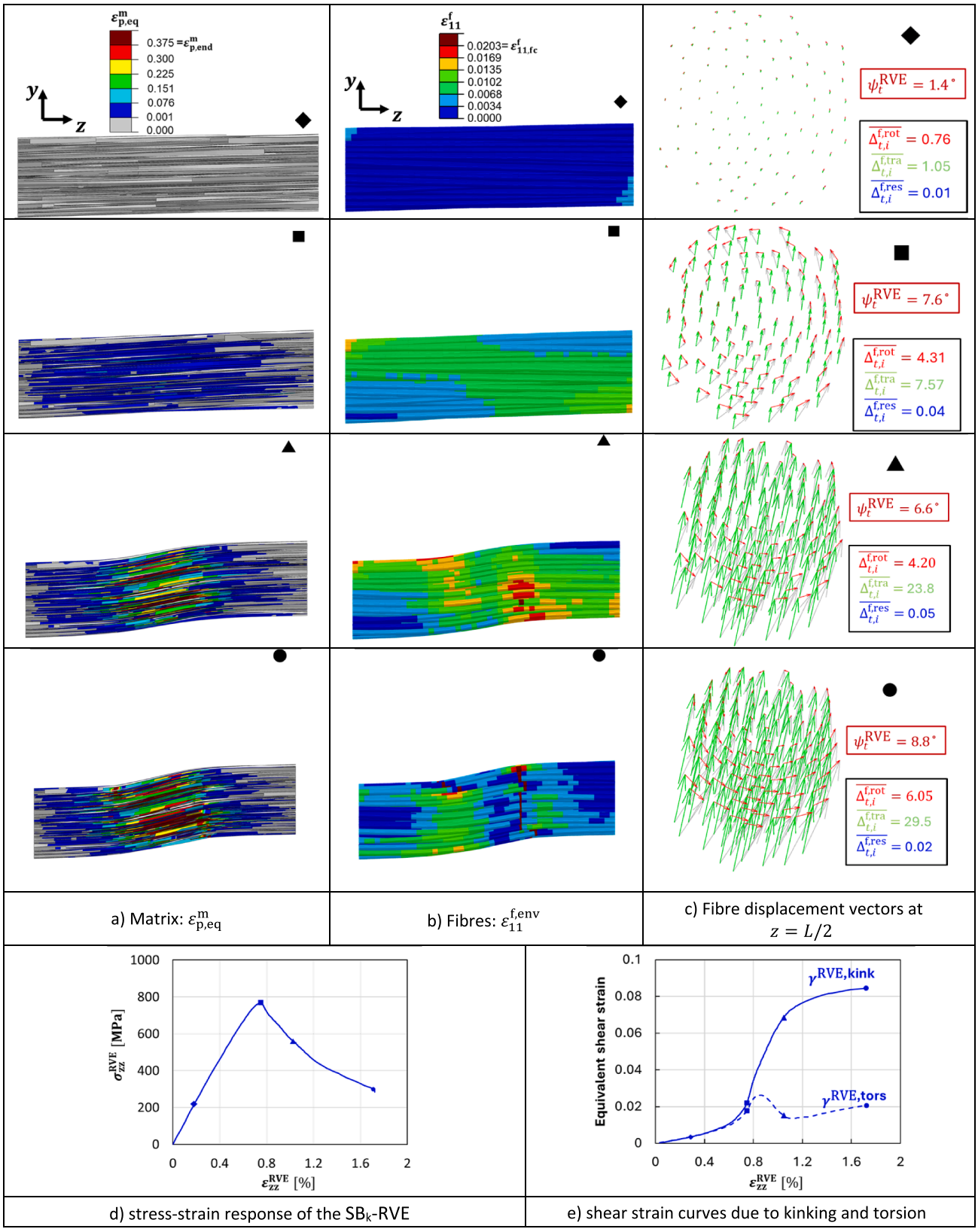


Fig. 19. Sequence of events of constituents (a-c) and composite's global response (d-e) during compression failure of the SB_k-RVE, shown at four characteristic increments (identified by the markers shown in the top-right corners of the images and the stress–strain curve in image d). Image c shows the Procrustes decomposition of deformation components as explained in Section 4.

1. It proposes new advanced microstructural metrics to characterise misalignment and twisting of fibres and RVEs, new deformation metrics to quantify kinking and torsion during compression, and analyses their relationships;
2. It presents a new methodology for generating continuum μFEM of RVEs with high fibre content (up to 55 %) and without unrealistic resin rich boundaries or fibre interpenetration;
3. It presents a thorough validation of our recently proposed, computationally-efficient shell-beam (SB) methodology at the microstructural level.

While addressing these challenges, the following conclusions have been drawn:

- The sequence of failure mechanisms under longitudinal compression includes not only kinking (i.e. shearing in the transverse direction), but also a torsional deformation. This coupling between compression, kinking and torsion evolves non-linearly during loading and can only be captured by fully 3D models, as 2D planar approaches inherently neglect torsion effects.
- Realistic microstructures are essential for accurately predicting the compressive performance of composites and assessing the influence of fibre imperfections. The inherently 3D nature of the mechanisms requires realistic 3D fibre paths. The coupling between kinking and torsion requires RVEs with appropriate matrix content and without artefactual matrix-rich boundary regions.
- The new combined metrics for analysing real FRP microstructural imperfections and micromechanical deformation modes confirm, for the first time at the micromechanical level, the well-established link between the direction of coordinated fibre misalignments and kinking. Moreover, these metrics reveal a previously unreported link between coordinated twisting of bundles of fibres and the coupling between compression and torsion.
- The SB_k variation offers the best combination of computational efficiency and accuracy for predicting the micromechanical features of the FRP compressive response. Its accuracy has been demonstrated against CC-μFEM in terms of homogenised stress–strain response, evolution of matrix plasticity, onset of fibre failure, and the development of kinking–torsion mechanisms.

Overall, the SB_k methodology and new microstructural metrics have the potential to help composite manufacturers assessing how microstructural imperfections introduced during different manufacturing stages influence compressive failure and overall composite performance. This provides a pathway towards using μFE simulations for quality assessment in composite manufacturing.

CRediT authorship contribution statement

D. Bikos: Writing – review & editing, Writing – original draft, Visualization, Methodology, Investigation, Formal analysis, Conceptualization. **R.S. Trask:** Writing – review & editing, Writing – original draft, Validation, Supervision, Funding acquisition. **P. Robinson:** Writing – review & editing, Writing – original draft, Validation, Supervision. **S. Pimenta:** Writing – review & editing, Writing – original draft, Visualization, Validation, Supervision, Project administration, Methodology, Investigation, Funding acquisition, Conceptualization.

Declaration of competing interest

The authors declare that they have no known competing financial interests or personal relationships that could have appeared to influence the work reported in this paper.

Acknowledgements

The authors kindly acknowledge the funding for this research provided by the UK Engineering and Physical Sciences Research Council (EPSRC) programme Grant EP/T011653/1, Next Generation Fibre-Reinforced Composites (NextCOMP): a Full-Scale Redesign for Compression in a collaboration between Imperial College London and the University of Bristol. For the purpose of open access, a Creative Commons Attribution (CC BY 4.0) license is applied to any author-accepted manuscript version arising.

Appendix A. Supplementary data

Supplementary data to this article can be found online at https://doi.org/10.1016/j.compositesa.2025.109515.

Data availability

Data will be made available on request.

References

[1] Wang Y, Emerson MJ, Conradsen K, et al. Evolution of fibre deflection leading to kink-band formation in unidirectional glass fibre/epoxy composite under axial compression. Compos Sci Technol 2021;213:108929.
[2] Emerson MJ, Wang Y, Withers PJ, et al. Quantifying fibre reorientation during axial compression of a composite through time-lapse X-ray imaging and individual fibre tracking. Compos Sci Technol 2018;168:47–54.
[3] Budiansky B, Fleck NA. Compressive failure of fibre composites. J Mech Phys Solids 1993;41:183–211.
[4] Gomarasca S, Peeters DMJ, Atli-Veltin B, et al. Characterising microstructural organisation in unidirectional composites. Compos Sci Technol 2021;215.
[5] Srisuriyachot J, Bénézech J, Couégnat G, et al. Synchrotron micro-CT in kink-band formation of UD-CFRP laminates with microdefects. Compos B Eng 2023;266:111038.
[6] Takahashi T, Ueda M, Iizuka K, et al. Simulation on kink-band formation during axial compression of a unidirectional carbon fiber-reinforced plastic constructed by X-ray computed tomography images. Adv Compos Mater 2019;28:347–63.
[7] Iizuka K, Ueda M, Takahashi T, et al. Development of a three-dimensional finite element model for a unidirectional carbon fiber reinforced plastic based on X-ray computed tomography images and the numerical simulation on compression. Adv Compos Mater 2019;28:73–85.
[8] Takahashi T, Todoroki A, Kawamura C, et al. Unidirectional CFRP kinking under uniaxial compression modeled using synchrotron radiation computed tomography imaging. Compos Struct 2022;289:115458.
[9] Bikos D, Poh F, Trask RT, et al. Shell-Beam micromechanical models: improving the computational efficiency of simulations of composites under longitudinal. Compos Struct 2025;354:118830.
[10] Emerson MJ, Jespersen KM, Dahl AB, et al. Individual fibre segmentation from 3D X-ray computed tomography for characterising the fibre orientation in unidirectional composite materials. Compos A Appl Sci Manuf 2017;97:83–92.
[11] Gomarasca S, Peeters DMJ, Atli-Veltin B, et al. Characterising pore networks and their interrelation with the fibre architecture in unidirectional composites. Compos A Appl Sci Manuf 2025;190:108669.
[12] Mesquita F, Bucknell S, Leray Y, et al. Single carbon and glass fibre properties characterised using large data sets obtained through automated single fibre tensile testing. Compos A Appl Sci Manuf 2021;145:106389.
[13] Wisnom MR. The effect of fibre misalignment on the compressive strength of unidirectional carbon fibre/epoxy. Composites 1990;21:403–7.
[14] Nunna S, Ravindran AR, Mroszczok J, et al. A review of the structural factors which control compression in carbon fibres and their composites. Compos Struct 2023;303:116293.
[15] Pimenta S, Patni M, Bikos D, et al. The role of constitutive properties on the longitudinal compressive strength of composites. Compos A Appl Sci Manuf 2024;108264.
[16] Pimenta S, Gutkin R, Pinho ST, et al. A micromechanical model for kink-band formation: part I - experimental study and numerical modelling. Compos Sci Technol 2009;69:948–55.
[17] Potter K, Langer C, Hodgkiss B, et al. Sources of variability in uncured aerospace grade unidirectional carbon fibre epoxy preimpregnate. Compos A Appl Sci Manuf 2007;38:905–16.
[18] The MathWorks Inc. MATLAB version: 24.1.0 (R2024a) 2024.
[19] Ueda M, Akiyama M. Compression test of a single carbon fiber in a scanning electron microscope and its evaluation via finite element analysis. Adv Compos Mater 2019;28:57–71.
[20] Sorini C, Chattopadhyay A, Goldberg RK. An improved plastically dilatant unified viscoplastic constitutive formulation for multiscale analysis of polymer matrix composites under high strain rate loading. Compos B Eng 2020;184:107669.
[21] Dassault Systèmes Simulia, Fallis AG. ABAQUS documentation. Abaqus 612 2013.

[22] Bishara M, Rolfes R, Allix O. Revealing complex aspects of compressive failure of polymer composites – Part I: Fiber kinking at microscale. Compos Struct 2017;169:105–15.
[23] Fisher NI. Statistical Analysis of Circular Data. Cambridge University Press; 1993.
[24] Eggert DW, Lorusso A, Fisher RB. Estimating 3-D rigid body transformations: a comparison of four major algorithms. Mach Vis Appl 1997;9:272–90.
[25] Lara-Curzio E, Garcia D. The Effect of Diameter Variation Along a Fiber on the Determination of Fiber Strengths and the Parameters of Their Distribution. 25th Annual Conference on Composites, Advanced Ceramics, Materials, and Structures: A: Ceramic Engineering and Science Proceedings, vol. 22, John Wiley & Sons, Inc.; 2001, p. 363–70.
[26] Tanaka T, Nakayama H, Sakaida A, et al. Estimation of tensile strength distribution for carbon fiber with diameter variation along fibre. J Soc Mater Sci, Jpn 1999;48:90–7.
[27] Imperial College Research Computing Service. High performance computing (HPC) 2023.
[28] Pimenta S, Gutkin R, Pinho ST, et al. A micromechanical model for kink-band formation: Part II-Analytical modelling. Compos Sci Technol 2009;69:956–64.
[29] Chamis CC. Mechanics of composite materials: past. Present and Future 1984.
[30] Wang Y, Chai Y, Soutis C, et al. Evolution of kink bands in a notched unidirectional carbon fibre-epoxy composite under four-point bending. Compos Sci Technol 2019;172:143–52.
[31] Hobbiebrunken T, Fiedler B, Hojo M, et al. Experimental determination of the true epoxy resin strength using micro-scaled specimens. Compos A Appl Sci Manuf 2007;38:814–8.
[32] Klavzer N, Abatour M, Chevalier J, et al. Modelling of size-dependent plasticity in polymer-based composites based on nano- and macroscale experimental results. Compos A Appl Sci Manuf 2024;185:108309.
[33] Gu X, Chen F, Yuan M, et al. Influence of matrix plastic properties on compressive strength of carbon fiber composites: a combined FEA and experimental study. Compos A Appl Sci Manuf 2025;198:109084.
[34] Quino G, Gargiuli J, Pimenta S, et al. Experimental characterisation of the dilation angle of polymers. Polym Test 2023;125:108137.